LAWRENCE
LIVERMORE
NATIONAL
LABORATORY

LLNL-CONF-666675

From micojoules to megajoules and kilobars to gigabar:probing matter at extreme states of deformation

B. Remington, R. Rudd, J. Wark

January 28, 2015

APS
New Orleans, LA, United States
October 25, 2014 through November 1, 2014

Disclaimer

From microjoules to megajoules and kilobars to gigabars: probing matter at extreme states of deformation*

Bruce A. Remington and Robert E. Rudd
Lawrence Livermore National Laboratory, Livermore, CA 94550 USA

Justin S. Wark
Department of Physics, Clarendon Laboratory, University of Oxford, Oxford, , OX1 3PU UK

Abstract

Over the past 3 decades there has been an exponential increase in work done in the newly emerging field of matter at extreme states of deformation and compression. This accelerating progress is due to the confluence of new experimental facilities, experimental techniques, theory, and simulations. Regimes of science hitherto thought out of reach in terrestrial settings are now being accessed routinely. High-power lasers and pulsed power facilities are accessing high-pressure macroscopic states of matter, and next-generation light sources are probing the quantum response of matter at the atomistic level. Combined, this gives experimental access to the properties and dynamics of matter from femtoseconds to microseconds in time scale and from kilobars to gigabars in pressure. There are a multitude of new regimes of science that are now accessible in laboratory settings. Examples include planetary formation dynamics, asteroid and meteor impact dynamics, space hardware response to hypervelocity dust and debris impacts, nuclear reactor component response to prolonged exposure to radiation damage, advanced research into light weight armor, and capsule dynamics in inertial confinement fusion (ICF) research. We will review highlights and advances in this rapidly developing area of science and research.

I. Introduction

There is an enduring interest in understanding the properties of matter at high pressures and compressions, driven partly by a desire to understand the structures and properties of planetary interiors, and their formation dynamics. An obvious example is our interest to understand the interior structure of the Earth, as illustrated by the phase diagram for iron in Fig. 1a. Understanding the phase and melt curve of iron at high pressure advances our understanding of the Earth, [Buffett 2000; Dziewonski 1981; Wang 2013] and Earth-like exoplanets, such as the so-called "Super-Earths". [Seager 2007; Schneider 2011; Valencia 2006, 2009; Swift 2012; Fortney 2009; Sotin 2007] In another arena, motivated by the requirements of the inertial confinement fusion (ICF) program, [Haan 2011; Edwards 2011, 2013; Rosen 1996, 1999, 2015] material properties, such as equations of state, opacities, reflectivities, and conductivities, have became important to know quantitatively over a very wide range extending from near ambient to very high pressures (kbars to gigabars). Furthermore, the requirements of the ICF ignition program drive the need to understand material properties to pressures as high as 100 Gbar (10^4 TPa) and compressions, ρ/ρ_0 , of a few up to as high as ~1000. This has opened up an experimental branch of science studying matter under conditions relevant to the interiors of planets and stars. Also, a new focus area of laboratory astrophysics at high energy density (HED) conditions has emerged. [Remington 1999, 2000, 2006a] The setting for these experiments are typically high-power lasers and magnetic pinch facilities. The energies of these drivers range from microjoules (in university laboratories) to megajoules (at the national laboratories). We review here the field of material science and material dynamics over these ranges of pressures and compressions. This work is distinct from, but complementary to, the work done on diamond anvil cells (DAC) to study material properties. The DAC experiments can reach high pressures,

up to ~600 GPa, but under quasi-static, isothermal conditions. [Dubrovinsky 2012] The work reviewed here is all dynamic (time resolved) and adiabatic, in the sense that heat created during compression or release largely remains within the samples studied. A remarkable result of this "extreme materials science" is the realization that one of the most useful theoretical and simulation tools for exploring these unique regimes of extreme pressures and rates of compression, namely, molecular dynamics (MD) simulations, occur over comparable spatial and temporal scales as the HED experiments. [Rudd 2010] This confluence allows reasonably direct comparisons between experiments and the classical (yet often quantum mechanically based) interatomic potentials that reside at the core of MD simulations.

This paper is organized as follows. In Sec. II, we start by giving an example of how the field of dynamic properties of materials started in the 1960s and 1970s. We describe a widely cited wave profile measurement of shock loaded iron based on powder gun driven plate impact in which the the α to ε (bcc to hcp) phase transition in iron was deduced. We also include in this section examples of modern laser and Z-pinch driven, ramp compression experiments on iron to measure wave shapes, and determine the α–ε phase transition stress as a function of strain rate. Then we describe in Sec. III the first time-resolved diffraction experiments, carried out in shocked single crystal Si on ICF class pulsed lasers. In Sec. IV, we review a series of high-rate, high-pressure experiments on copper, a face-centered cubic (fcc) metal. Then in Sec. V we describe time resolved diffraction experiments on shocked iron, in which the α to ε (bcc to hcp) phase transition was observed for the first time at the lattice level. Section VI presents the results of diffraction experiments on ramp loaded MgO at very high pressures, and directed towards the understanding of planetary interior structure. We describe in Sec. VII the first dynamic extended x-ray absorption fine structure (EXAFS) measurements on shocked vanadium to deduce temperature and density behind the shock, and shocked iron to infer the phase. In Section VIII, we describe EXAFS measurements on off-Hugoniot iron loaded to peak pressures approaching 600 GPa (6 Mbar). Then Sec. IX presents a series of high-pressure experiments in Ta, integrated and at the lattice level, including a discussion of a Ta multiscale strength model. Sec. X presents results of experiments to measure the entropy on the Hugoniot in shocked SiO_2 and to determine its vaporization curve on release. In Sec. XI, results describing ramp compression experiments of carbon to 5 TPa (50 Mbar) peak pressures, and comparisons with a number of theoretical calculations are presented. We describe the development of experiments to study the properties of matter at pressures approaching 100 TPa (1 Gbar) in Sec. XII. We finish with a short conclusion in Sec. XIII.

II. Compression Wave Profile Experiments in Iron

Reaching the regimes required to study the properties of matter at Earth interior conditions requires high pressures and high densities, as illustrated in Fig. 1a. [Wang 2013] To study iron at Earth core conditions will requires reaching pressures of 300-400 GPa at temperatures of 5000-6000 K, which is near to but just below the melt temperature at these pressures. A promising experimental approach for reaching these conditions is an initial strong shock followed by ramp compression to the required pressures and temperatures. [Wang 2013] We first describe below an early experiment to shock iron using plate impact experiments, followed by more recent work on developing the required ramp compression part of the loading to reach the highest pressures without melting the iron.

The study of the dynamic behavior of matter was pursued in the 1970s with experiments using plate impact techniques to produce planar shocks in samples and measuring the resulting free-surface velocities with Velocity Interferometer System for Any Reflector (VISAR) diagnostics. The free-surface velocity measurements in shocked iron provided the first suggestion of a shock

driven polymorphic phase transition in iron at a shock strength of around 13 GPa, which was interpreted as the α–ε (bcc-hcp) transition. An example of such a free surface velocity measurement for shocked iron using a powder gun to generate a plate impact is shown in Fig 1b, for a peak shock stress of 23.7 GPa. [Barker 1974] The structure in this velocity profile corresponds to the elastic precursor (E), the first plastic wave (P1) corresponding to the onset of the transition from the α to the ε phase, the second plastic wave (P2) corresponding to "the wave which carries the material from the α phase to the peak stress level in the ε phase", and the phase interface reflection (PIR) wave, which is an artifact of reflecting off a free back surface. [Barker 1974] The measurement, and its predecessor by Bancroft [Bancroft 1956], helped kick off the field of dynamic properties of matter.

More recent generations of experiments have focused on developing off-Hugoniot ramp wave loading techniques, to be able to study the properties of matter in the solid state at much higher pressures. Figure 1c shows a free-surface velocity versus time measurement from such a ramp wave experiment done on iron [Smith 2013] at the Sandia Z-machine [Matzen 2005]. The velocity plateau at $u_{fs} \sim 0.75$ km/s is attributed to the onset of the α–ε phase transformation in iron. An interesting observation, shown in the inset, is that the α–ε phase transition velocity plateau decreases with time, as a result of the time dependence of the transition, that is, phase transition kinetics. When more time is available for the phase transition to occur, its onset is observed at a slightly lower uniaxial loading stress. This point becomes important when looking for phase transitions in high rate loading environments, where high pressure conditions in the sample can only be held for short durations of time.

To more fully explore the effects of loading rates on wave profile evolution in ramp compressed iron, a compendium of results is shown in Fig. 1d, [Smith 2013] from experiments done on the Janus [Wark 1989] and Omega [Boehly 1997] lasers, a micro-joule laser at LLNL, [Crowhurst 2014] and the Z pulsed power facility. What is plotted is the uniaxial loading stress required to initiate the α–ε phase transition in iron, as a function of the strain rate associated with the transition. This figure is particularly noteworthy, because it shows that the higher the loading rate, the higher the observed α–ε phase transition stress. Above a strain rate of $\sim 10^6$ s^{-1}, this effect is particularly significant. The inset of Fig. 1d shows a similar effect, only for the peak elastic precursor stress, marking the onset of plastic flow in iron. The sudden increase of elastic – plastic transition stress at strain-rates $> \sim 10^6$ s^{-1} is suggested to result from a transition from thermal activation to a phonon drag regime of plastic flow. [Smith 2013]

III. Diffraction on Shocked Silicon

The first time-resolved, dynamic diffraction experiments using an ICF class laser, the Janus laser at LLNL, launched a ~7 GPa (70 kbar) shock through a 250 μm thick single crystal sample of [111] Si, as shown in Fig. 2. [Wark 1987, 1989] The experimental configuration is shown in Fig. 2a, and time resolved diffraction data showing a shock compressed lattice is given in Fig. 2b. The drive was generated by direct illumination of a 1 ns FWHM Gaussian pulse of 1 μm light at an intensity of $\sim 4 \times 10^9$ W/cm^2. A second synchronized but delayed laser beam, 10 J at a wavelength of 0.53 μm and a 100 ps Gaussian pulse shape, generated a burst of Ca He-α x-rays at ~3.9 keV to record a time-resolved Bragg diffraction signal, which measured the lattice response to the shock in Si. As the diffraction signal was recorded from a single plane, the data were not sufficient to differentiate whether the observations corresponded to a one dimensional (1D) elastic compression or a three dimensional (3D) relaxed plastic compression. Nevertheless, the ability to do time-resolved, nanosecond scale, microscopic, lattice level measurements of the crystal response to a "strong" shock (in the sense of a stress of order tens of kbar) had now been

experimentally demonstrated.

A decade later on the Nova laser, an experiment using an x-ray drive acquired a more substantial set of data reaching higher shock pressures, as shown in Fig. 3. [Loveridge-Smith, 2001] The experimental configuration used a hollow cylindrical Au radiation cavity ("hohlraum"), as shown in Fig. 3a, to convert the 351 nm drive laser into a Planckian radiation drive of radiation temperatures $T_r \sim 20$-60 eV. This radiation was used to launch shocks of 19, 26, and 60 GPa strength along the [400] direction of the single crystal Si. The diffraction from the (400) lattice plane in the direction of the shock velocity was streaked in time, to give continuous time coverage, as shown in Fig. 3b. The time-averaged diffraction profile for each shock from the (400) lattice planes are shown in Fig. 3c. The stronger the shock, the smaller the normalized lattice spacing, d/d_0, where d and d_0 correspond to the lattice spacing for the shocked and unshocked lattice planes. The corresponding patterns for diffraction from the (040) lattice planes, transverse to the direction of shock motion, are shown in Fig. 3d. These transverse lattice planes showed no observable lattice compression, even once the compression wave had reached the rear surface of the sample. This was interpreted as demonstrating that on the nanosecond time scales of the experiment, the shocked single crystal Si did not have time to evolve plastically to a 3D relaxed state; the observed diffraction was consistent with a 1D elastic compression, with the (040) lattice spacing transverse to the [400] shock direction remaining unchanged over the ~2 ns of the experiment. The sharpness of the (040) diffraction peaks shown in Fig. 3d confirmed the low density of dislocations and other shock-induced lattice defects, at least within the leading region of the compression wave profile. Recent MD simulations [Mogni, 2014] suggest that following the initial elastic wave the Si may have undergone a transition to a mixed phase (which, owing to the lattice constant of the new phase relieves the large shear stresses without the need for conventional plastic flow). This forms crystallites sufficiently small that the associated diffraction peaks were too broad to have been observed in the experimental geometry. That said, those MD simulations still do not seem to be able to predict correctly many aspects of the experimental results. Remarkably, after many years of study, full knowledge of the nanosecond response to compression of one of the purest, defect-free, crystals known remains elusive.

IV. Diffraction on Shocked Copper

In the same work by Loveridge-Smith, [Loveridge-Smith, 2001] a 2 μm thick single crystal Cu sample was shocked at a strength of ~18 GPa along the [200] direction, and Bragg diffraction signals were recorded from the (200) and (020) face-centered cubic (fcc) lattice planes (not shown). The shock was generated by direct illumination ("direct-drive") of the laser on the single crystal Cu sample on the Omega laser. In these shocked Cu experiments, the lattice promptly relaxed plastically such that the lattice spacing in the transverse (020) direction and the shocked axial (200) direction were nearly the same. Estimates based on Orowan's equation,

$$d\varepsilon_p/dt \sim \rho_{disloc} v_{disloc} b, \qquad (1)$$

where ε_p, ρ_{disloc}, v_{disloc}, and b correspond to plastic strain rate, mobile dislocation density, average dislocation velocity, and Burger's vector, suggest that the dislocation density behind the shock was high, $\rho_{disloc} \sim 10^{11}$-$10^{12}$ cm^{-2}, and that these dislocations were sufficiently mobile so as to relieve the shear stress within a few hundred picoseconds. Such a response is consistent with the lower Peierls stress for the metallic fcc Cu than for the covalently-bonded diamond-cubic Si. However, the time resolution of the shocked Cu experiment performed on the Omega laser was insufficient to actually resolve the relaxation time.

Our understanding of the response of a simple fcc metal such as Cu has been greatly enhanced by the development of large scale molecular dynamics (MD) simulations, which now can encompass the time (nanosecond) and length (micron) scales of the laser-based experiments. The initial MD simulations [Holian 1998], constrained to only a few tens of picoseconds, demonstrated the rapid generation of defects in shocked fcc metals, but did not capture the full 1D to 3D relaxation seen in the experiments discussed above, as plasticity occurs via the subsequent motion of these dislocations. [Rosolankova 2004] With rapid developments in computing power, larger and longer simulations of shocked single crystal [100] Cu were carried out, as shown in Figs. 4a [Bringa 2006] using the embedded atom model (EAM) interatomic potential by Mishin [Mishin 2001]. These simulations enabled the 1D-3D relaxation time scale, $\tau_{1D\text{-}3D}$, to be studied numerically as a function of shock front rise time (0 ps vs. 50 ps). The shock strength was 35 GPa, whereas the homogeneous (dislocation) nucleation threshold was observed in the simulations to be ~30 GPa. One of the main conclusions of this MD simulation study was that the plastic relaxation time behind the shock, $\tau_{1D\text{-}3D}$, was of order ~30 ps., as shown in Fig. 4b giving the time evolution (relaxation) of the shear stress behind the shock. Above the homogenous nucleation threshold, for the steep shock front (0 ps rise time), the dislocation density behind the shock was high, ~$3x10^{13}$ cm^{-2}. In simulations with pre-existing sources (dislocation loops), and a ~50 ps rise time on the shock front, the final dislocation density was about a factor of 3 lower at ~$1x10^{13}$ cm^{-2}. The relaxation times were similar, however, suggesting a higher average dislocation velocity for the ramped shock case. This also led to the prediction that, even in the case of real metals with initial defects, elastic response right up to the ultimate theoretical uniaxial compressive strength of the material should be attainable on timescales of tens of picoseconds.

The ground-breaking diffraction experiments described above were performed with quasi-monochromatic x-ray sources emitted from plasmas created by high-intensity optical pulses synchronous to the pulse launching the shock in the sample. The duration of the probe x-ray sources ("backlighters") were limited mainly by the duration of the optical laser pulse, which in most cases ranged from 100 ps to 1 ns. However, with the advent of Free Electron Lasers such as the Linac Coherent Light Source (LCLS) at SLAC, it is now possible to make shock diffraction measurements with better than 100-fsec time resolution – i.e. shorter than the period of the fastest phonon in the system. Furthermore, the bandwidth of the x-rays is of order a few times 10^{-3}, and can be reduced further by monochromating crystals. A recent experiment was performed using the Coherent X-ray Imaging Instrument (CXI) at LCLS to study time-resolved powder diffraction from shocked polycrystalline Cu, for a shock strength of ~70 GPa. [Milathianaki, 2013] These polycrystalline samples had an average grain size of ~400 nm, and were highly textured, with a dominant <111> orientation normal to the target surface, which is also the direction of the shock compression wave.. The experimental setup for this experiment is shown in Fig. 4c, and simulations that reproduce the analyzed experimental results are shown in 20 ps steps in Fig. 4d. The time evolution from a 1D elastically compressed lattice to a more 3D relaxed lattice spacing is evident. Further calculations shown in Fig. 4e more clearly quantify the onset of plasticity, with curves of normal elastic strain, transverse plastic strain, and transverse elastic strain vs. time. The time lag between the elastic compression and the onset of plastic response is ~50-70 ps, and occurs only when the normal elastic strain in the [111] direction has reached ~18%. This ~50 ps 1D-3D relaxation time scale is reasonably close to the MD predictions of ~30 ps from MD simulations, albeit for a 35 GPa shock in single crystal Cu sample. This same analysis of the experimental data gives a shear stress (strength) of ~10-20 GPa. In Fig. 4f, the results of a set of MD simulations are shown, giving stress-strain curves for compression of Cu along the [123], [110], [111] and [001] directions at a temperature of 300 K and strain rate of 10^8 s^{-1}. [Dupont 2012] The strain threshold for dislocation nucleation (onset of plasticity) is indicated with arrows. For the [111] compression, an elastic strain of 16-20% is predicted before

the transition to a plastically relaxed state, with a peak shear stress of τ_{shear} ~ 15-20 GPa, in good agreement with the LCLS experiment of shocked Cu (Fig. 4e). What is remarkable about these results is that the temporal and spatial scales of the various MD simulations and the LCLS experiment match, and the predicted relaxation times are in reasonable agreement. This is a noteworthy achievement for the study of shocked solid-state samples, bringing state-of-the-art simulations and experiments into one-to-one comparison in temporal and spatial scales, without the need for any scaling. It is also a rather significant demonstration that these MD simulations using EAM potentials appear to be a reasonably good representation of experimental reality, provided very large scale simulations are undertaken.

V. Diffraction on Shocked Iron

The next dynamic diffraction experiments we describe were aimed at looking at phase, in particular, looking for solid-solid phase transitions. We show in Figs. 5a and 5b the first dynamic (time resolved) diffraction experiment to conclusively show the iron α to ε (bcc to hcp) phase transition at the lattice level in shocked iron. [Kalantar 2005; Hawreliak 2006; Wark 2007] The raw diffraction image for single crystal Fe shocked at 26 GPa along the [001] direction is shown in Fig. 5a, with the lattice planes identified. The diffraction arcs for unshocked material are labeled in blue. The arcs corresponding to elastically compressed bcc Fe are labeled in green, and the diffraction arcs corresponding to compressed hcp Fe are labeled in red. Peak uniaxially applied pressure vs. observed compression for an extensive series of shots for shocked single crystal Fe are plotted in Fig. 5b. Experiments from the Vulcan laser (red), Janus laser (green), and Omega laser (blue) are shown. For compressions up to ~6%, the experimental diffraction data show that the crystal response is a 1D elastically compressed bcc lattice. Then there is a volume collapse, and the compression jumps to 15-18%, corresponding to the transition to an hcp lattice, consistent with the α–ε phase transition occurring for a shock strength of ~13 GPa (130 kbar). The time scale for this transition to occur is less than the ~2 ns time resolution of this experiment.

A set of large-scale MD simulations preceded the experiment, [Kadau 2002, 2005], examples of which are shown in Figs. 5c and 5d. The simulation result (Fig. 5c) shows unshocked Fe (gray), a region of 1D uniaxial elastic shock compression (blue), and 3D relaxed hcp phase Fe (red), with grain boundaries shown in yellow, for a 15 GPa shock. Of particular note is that there is no plastic region in the shocked bcc Fe lattice. The elastically compressed bcc lattice transforms directly to the hcp relaxed Fe lattice, which is similar to what was observed in the laser-driven shock compression experiments shown in Figs. 5a and 5b. Figure 5d shows yet another important result from the MD simulations. The α – ε transition for the 15 GPa shock in the MD simulations was very fast, requiring only ~2 ps to transform. The experiments also observed that this phase transition is fast, but only had ~2 ns time resolution, so could not establish how fast. Both simulation and experiment are consistent with a compression and shuffle mechanism responsible for the phase change from bcc to hcp. [Hawreliak 2006] Also both show a highly-oriented nanocrystalline structure of very small grain size (grain sizes of 2-15 nm) after the phase transition, due to the four degenerate directions in which the phase change can occur. [Hawreliak 2008]

Later experiments performed on polycrystalline iron [Hawreliak 2011] where the shock-induced phase transition was also observed, did show clear evidence for plasticity, presumably due to a combination of the effects of grain boundaries as sources of dislocations, and because the sample contained randomly oriented crystallites. It is also important to note that whilst MD and experimental length and time-scales are now

converging, the faithfulness of the simulations is dependent upon the fidelity of the potentials used, and in the case of shock compression, a good model of the system is required over a large range of compressions. This may explain why some predictions made by MD - such as a large fraction of fcc phase in iron shocked along other axes [Kadau 2007] - have not to date been seen experimentally.

VI. High Pressure Diffraction on Ramp Compressed Magnesium Oxide

We next describe a very high-pressure dynamic diffraction experiment for ramp compressed magnesium oxide (MgO), at peak pressures of up to 900 GPa (9 Mbar). [Coppari 2013] These experiments were motivated by an interest to understand material properties and phases at the high pressures relevant to planetary interiors, including the newly discovered super-Earths. [Schneider 2011; Seager 2007] MgO was chosen as an important component of the Earth's mantle and likely important for other planets. Little is known about the behavior of this oxide under conditions expected in the super-Earths with masses significantly greater than the mass of the Earth, where pressures can exceed 1,000 GPa (10 Mbar). [Valencia 2006, 2009; Swift 2012; Fortney 2009; Sotin 2007]

The ambient phase of MgO is the NaCl-type rocksalt structure (denoted B1), and this phase is predicted to remain stabile over a significant range in pressure and temperature. [McWilliams 2012] A phase transition from the six-fold coordinated B1 to the eight-fold coordinated CsCl-type (B2) structure is theoretically predicted in the 400–600 GPa range. With the existence of high energy lasers from ICF, these high pressure states of matter can now be experimentally probed. Experiments were carried out at the Omega Laser Facility, using direct laser illumination onto targets of 10-μm-thick MgO powder pressed between two diamond "anvils", as shown in Fig. 6a. [Coppari 2013] The drive lasers used a temporally shaped laser pulse shape with intensity increasing over ~4.5 ns, producing a ramped pressure wave. A VISAR velocity interferometer recorded the free-surface velocity versus time at the back of the rear diamond anvil, establishing the pressure versus time applied to the MgO sample. A Cu backlighter foil is irradiated using additional lasers with a 1 ns square pulse shape to produce quasi-monochromatic He-α radiation 8.3-8.4 keV incident at 45 deg. Diffracted x-rays are recorded in transmission geometry by image plates lining the inner walls of the diagnostic box, as shown in Fig. 6a.

The results from these diffraction experiments were analyzed to identify the lattice planes corresponding to the diffraction peaks, and to deduce the lattice spacing, as a function of pressure, as shown in Fig. 6b. These results show an abrupt change of lattice and spacing at 563 GPa, consistent with a phase transition from the B1 to B2. The MgO then remains in the B2 phase to the highest pressures achieved in these experiments, namely, 900 GPa. [Coppari 2013] The density of the solid MgO up to 900 GPa was determined by assuming the B1 phase up to 563 GPa then the B2 structure at higher pressures. Previous experimental density measurements were limited to pressures of ~200–250 GPa for the solid phase, based on gas gun shock experiments and static x-ray diffraction. This data set extends the experimentally explored pressure range considerably, reaching 2.4-fold compression for solid MgO.

This work experimentally shows that a solid–solid phase transition, consistent with a transformation from B1 to the B2 structure, occurs near 600 GPa, and that the B2 structure remains stable to 900 GPa. The results shown are relevant to planetary science, because these conditions are expected to exist in the deep interiors of planets more massive than the Earth. This work also demonstrates that solid–solid phase transitions at these high pressures (600 GPa) can occur on short timescales (a few nanoseconds).

VII. EXAFS on Shocked Vanadium and Iron

We now discuss a time-resolved microscale diagnostic developed to probe the local lattice response, namely, dynamic extended x-ray absorption fine structure (EXAFS). This EXAFS technique probes the lattice short-range order, works both with polycrystalline or single crystal samples, and offers the potential to infer phase, compression, and temperature of the loaded sample, with sub-nsec time resolution. [Konningsberger 1988; Lee 1981; Yaakobi 2003] When an atom absorbs an ionizing, high-energy x-ray, an electron rises from a bound state into the continuum. The outgoing wave packet of the free electron scatters off of neighboring atoms. The outgoing and reflected waves interfere with each other. The square of the total electron wave function is what determines the probability of the process, and this interference is therefore observed in fine structure in the x-ray absorption just above an opacity edge. For K-edge absorption, the standard EXAFS equation can be written, in terms of the normalized absorption probability, as [Konningsberger 1988; Yaakobi 2003, 2004a, 2004b]

$$\chi(k) = \Sigma_j \frac{N_j}{kR_j^2} F_j(k) \sin\{2kR_j + \phi_j(k)\} e^{-2\sigma_j^2 k^2} e^{-2R_j/\lambda(k)} , \qquad (2)$$

where $\chi(k) = [\mu(k) - \mu_0(k)] / \mu_0(k)$, and $\mu_0(k)$ represents the smooth absorption above the edge corresponding to an isolated atom (no interference modulations). The summation is over coordination shells, N_j is the number of atoms in the shell, and R_j its radius. The $F_j(k)$ factor corresponds to the backscattering amplitude for the electron wave function reflected from the jth coordination shell. The $\phi_j(k)$ represents a phase shift due to the electron wave packet moving through a varying potential. The exponential, $e^{-2\sigma_j^2 k^2}$, represents amplitude damping due to the Debye-Waller factor, which reduces the coherent interference of the EXAFS signal due to thermal and static disorder fluctuations in the local scattering atoms, and allows the lattice temperature to be measured, albeit volumetrically through the sample. The $e^{-2R_j/\lambda(k)}$ factor represents the attenuation of the electron wave function due to the finite mean free path, $\lambda(k)$, of the ejected electron.

A time-resolved EXAFS diagnostic technique has been developed at the Omega laser; [Yaakobi 2003] , 2004a, 2004b] the experimental setup is shown in Fig. 7a. Three 1-ns-square laser beams stacked back to back to make a 3-ns-square drive pulse are used to shock compress the sample being studied. The samples described here are either 10 μm thick polycrystalline vanadium or iron foils embedded in 17 μm thick CH tamper on either side, and the remaining 57 beams implode an inertial confinement fusion (ICF) capsule. This implosion generates a short (~150 ps) burst of smoothly varying hard x-rays, $I = I_0 \exp(-E_x/T)$, to be used for the EXAFS absorption. [Yaakobi 2003]

EXAFS measurements from shocked polycrystalline vanadium at $P_{shk} \sim 35$ GPa, together with EXAFS theoretical fits, using the FEFF8 code, [Behr 2000; Yaakobi 2004a, 2004b] are shown in Fig. 7b. Vanadium was picked as a good reference material, since at that time it was not expected to undergo any phase transition at shock pressures < ~100 GPa. Subsequently a rhombohedral phase transition in vanadium was discovered at ~65 GPa [Ding 2007], but the new phase does not affect the results shown here. The fits of the shocked vanadium EXAFS data with the FEFF8 code shown in Fig. 7b are very good, and suggest a compression of ~15% and shock temperature of ~770 K. Both the shock

compression and shock temperature thus inferred are in good agreement with predictions with radiation-hydrodynamics code simulations using the LASNEX code. [Zimmerman 1975]

Shocked polycrystalline iron experiments were also done with this dynamic EXAFS technique. [Yaakobi 2005a, 2005b] A 20% compression is predicted from radiation-hydrodynamics simulations of shocked Fe at $P_{shk} \sim 35$ GPa, assuming the α - ε phase transition. The FEEF8 theory was used to establish the expected EXAFS spectra for unshocked α-phase (bcc) Fe and shocked ε-phase (hcp) Fe, assuming a ~20% compression for the shocked state. Figure 7c (red curve) shows the experimental result for shocked Fe, and clearly shows that the small peak marked "w" in the α-phase disappears in the ε-phase. Based on these results, the observed data are consistent with the α - ε phase transition of shocked Fe, and that the transition time scale at $P_{shk} \sim 35$ GPa is $\tau_{\alpha-\varepsilon} < \sim 150$ ps, where 150 ps is the time resolution of this measurement. [Yaakobi 2005a, 2005b]

VIII. High Pressure EXAFS on Ramp Compressed Iron

Dynamic EXAFS spectroscopy measurements have also been done or staged-shock ramp compression of iron up to 560 GPa (5.6 Mbar), as shown in Fig. 8a. [Ping 2013] In these experiments, density, temperature, and local-structure measurements were made simultaneously for the compressed iron. The data show that the hexagonal close-packed (hcp) structure is stable up to 560 GPa. The temperature at peak compression is high and is explained as the result of a high dynamic strength of iron. These results also provide a constraint on the melting line of iron above 400 GPa.

The experiments were performed on the OMEGA laser and the broadband x-ray backlighter was generated by a spherical implosion. The target was a 4 μm thick Fe foil sandwiched between two diamond plates, each 35 μm thick, as shown by the experimental configuration in Fig. 8a. The diamond "anvils" confine the sample and maintain the pressure, thus creating a more spatially uniform compression state in Fe. The applied stress versus time in the Fe sample, using a temporally shaped laser pulse shape, is determined by simultaneous VISAR measurements. The laser energy and the delay between the drive and the backlighter were varied in a series of experiments to probe different pressures and temperatures in the Fe. The pressure equilibration in the thin Fe samples is confirmed by hydrodynamic simulations using LASNEX [Zimmerman 1975]. The short duration of the x-ray backlighter (~150 ps) ensures little temporal variation in the state of Fe during EXAFS measurements. [Yaakobi 2003]

The temperature dependence of EXAFS measurements occurs through the Debye-Waller factor effect, as mentioned regarding Eq. 1. [Di Cicco 1994; Zhu 1987; Higginbotham 2009; Yaakobi 2004b, 2005b]. The temperatures obtained in the high pressure EXAFS data are shown in Fig. 8b as a function of stress in the Fe. The data indicate that off-Hugoniot states have been achieved up to 560 GPa and 8000 K. The data fall into two groups based on the compression history: single shock (blue diamonds), and leading shock stress of ~150 GPa followed by staged compression waves (black triangles). The two single-shock points agree well with the calculated Hugoniot. The staged shock data show higher temperatures compared to the isentropes calculated for ramp compression following an initial 150 GPa shock, but ignoring material strength, and lower temperatures than those for a single shock Hugoniot at the same pressure.

The measured temperatures are higher than those calculated for the isentrope in Fig. 8b due to the added heating caused by doing work against the solid-state material strength in Fe during

compression at high pressure and strain rate. If one assumes that 100% of the work done against strength in compression goes into heat, the strength can be inferred from the measured temperatures. This is illustrated by the dotted and dashed black curves in Fig. 8b. The dotted curve fits the static strength results from 50 – 270 GPa pressures from Hemley et al. [Hemley 1997], and extrapolates the fitted result to 600. The added heating from this analysis, is not enough to reproduce the experimental EXAFS temperature measurements. It is well known now that the strength of ductile metals increases significantly due to the high strain rates of dynamic compression, as will be discussed in the Sec. IX below. [Barton 2011; Rudd 2010,2012,2014] To better match the experimental data, the "dynamic strength" is approximated by multiplying the static strength by a constant factor treated as a fitting parameter. The best fit result, shown by the dashed curve in Fig. 8b, corresponds to a multiplier of 3, than is, $Y_{dynamic} \sim 3Y_{static}$. The inferred strengths were on the order of 60-80 GPa (600-800 kbar), at pressures from 200 – 500 GPa.

IX. High Pressure Material Strength Experiments

Beyond the important questions of the compressibility and the phase diagram of materials at high pressure, the shear flow behavior of materials has been the subject of increasing interest [Rudd 2010]. The ability of a material to resist plastic (irreversible) flow is called material strength. Strong materials do not undergo plastic flow until higher stresses are applied. The vast majority of research on material strength has been near ambient conditions and at low rates. The shear stresses generated readily in plane-wave compression experiments using high-energy lasers or pulsed-power drives are more than sufficient to cause materials to yield. Once a material has yielded plastically, the strength of a material continues to be manifest in the flow stress, a measure of the shear stress during continued deformation. The flow stress is affected by the temperature and pressure, and it is also affected by the amount of the material has been strained plastically and the rate of deformation. The rise of the flow stress due to the accumulated plastic strain is known as work hardening. A well-known example is the increase in the strength of steel work hardened by a blacksmith hammering. The same effect is occurs as metals are driven to high pressure in plane-wave compression. The initially one-dimensional loading in a planar compression wave induces a large shear stress that drives plastic flow and leads to significant plastic strains.

There are a number of constitutive models that are widely used to calculate material strength (flow stress) in a fashion that can be incorporated into hydrodynamics continuum simulations. We will mention only four of the models used in the community. A more extensive review of the models can be found elsewhere. [Remington 2004, 2006b] The Steinberg-Guinan model assumes that high-pressure, high-strain-rate strength can be approximated as the ambient strength multiplied by a pressure and temperature sensitive factor which is assumed to scale with the shear modulus, and a work hardening factor which is a power law function of strain. [Steinberg 1980] The Steinberg-Lund model adds in an explicitly strain rate dependence, and explicitly includes the effects of thermal activation and phonon drag. [Steinberg 1989] The Preston-Tonks-Wallace (PTW) model was developed specifically to address very high strain rate phenomena, and treats the thermal activation and phonon drag effects in a mathematically more sophisticated fashion. [Preston 2003] And finally, the Livermore multiscale strength model (LMS), described in more detail below in Sec. IX.B, is based on information transfer from quantum density functional theory (DFT) to molecular dynamics (MD) simulations of dislocation mobilities, to dislocation dynamics (DD) simulations of the evolution of the full dislocation ensemble, finally to the continue hydrodynamics scale. [Barton 2011] As such, the LMS is more closely tied to first principles theory, but at the price of being much more computationally demanding to assemble or modify.

The strength of a material at high pressure is of interest because of the effect it can have on material dynamics. In the propagation of a plane wave, it is the longitudinal stress that enters the equations of motion, so it is not the pressure alone but the sum of the pressure and the shear stress that matters. Knowing the flow stress of a material provides this important addition to the equation of state (the pressure). The flow stress also affects hydrodynamic instabilities such as the Rayleigh-Taylor instability [Barnes 1974; Colvin 2003; Robinson 1989; Swegle 1989]. If a low-density material pushes against and accelerates a high-density material, the interface between the two materials is unstable to the growth of small perturbations, due to the Rayleigh-Taylor instability. Consider a layer of water above a layer of air. The low-density air pushes on the higher-density water due to gravity. Quickly small perturbations on the interface grow, and bubbles of air rise through the water as spikes of water fall through the air. The same effect can take place in solids as a low-density fluid accelerates a high-density solid, but the strength of the solid acts to reduce the effect, suppressing the growth of perturbations at short wavelengths and in some cases restoring stability. Rayleigh-Taylor instability is a potential source of detrimental mixing in ICF [Ma 2013], and the use of strong materials may provide a means of controlling the mixing. [Barnes 1974]

Several approaches have been developed to determine the strength of materials in high-pressure dynamic experiments. If the equation of state were known perfectly, the longitudinal stress determined by surface velocimetry (VISAR) would imply the flow stress. In practice, expressing the flow stress in terms of the difference of the pressure and the longitudinal stress relies on the difference of two large numbers, and uncertainties in the equation of state are often comparable to the flow stress: a more sophisticated technique is needed. Here we discuss three approaches to determining the flow stress that are designed to minimize the impact of uncertainty in the equation of state. The first approach uses the Rayleigh-Taylor growth of pre-imposed ripples on an accelerated interface to infer the flow stress. The second uses x-ray diffraction to measure the shear strain at the atomic level. The third measures the transit across the yield surface as the compression peaks and then the material releases. A forth technique was already discussed in Fig. 7b, where temperature is measured by dynamic EXAFS, and the heating beyond the isentrope is equated with the work done against the material strength (flow stress). [Ping 2013]

IX.A. Rayleigh-Taylor Strength Experiments

Experiments to infer the flow stress at pressures of ~100 GPa have been conducted on metals at the Omega laser in Rochester and experiments have started at the National Ignition Facility. [Park 2015] The experiments use face-on x-ray radiography to measure the growth of pre-imposed ripples on the surface of the metal as it is accelerated by a material with much lower density. The configuration of the experiment is shown schematically in Fig. 9a. Laser beams enter a gold hohlraum where they generate an intense x-ray radiation bath. The x-rays strike a plastic ablator, generating a shock wave that runs through a graded-density reservoir composed of materials such as brominated plastic (BrCH). As the shock breaks out from the surface of the reservoir, it creates plasma that crosses a vacuum gap and stagnates against the plastic heat shield on the far side, in a technique first introduced by Barnes et al. [Barnes 1974] for high-explosive driven Rayleigh-Taylor experiments. The resulting ramp-compression wave accelerates the rippled interface between the plastic heat shield and the metal. The growth of these ripples is measured at an instant in time using x-rays generated from a metal foil as short-pulse laser beams from the Omega EP laser strike it. A LiF tamper is used on the back side of the metal sample to maintain high pressure.

The most thorough Rayleigh-Taylor (RT) strength experiments to date have been performed on the body-centered cubic metals vanadium [Park 2010a, 2010b] and tantalum [Park 2012, 2015].

In each case a series of experiments has been conducted keeping the drive constant but changing the timing of the backlighter to map out the time evolution of the growth of the ripples. The drive itself is determined from VISAR on a separate laser shot at the beginning of the day. The measured ripple growth factors for a series of Ta RT experiments with a peak pressure of 100 GPa (1 Mbar) are plotted in Fig. 9b. The growth factor is the ratio of the final ripple amplitude to the initial ripple amplitude, as determined from radiography (ρR) using the procedure described in Park et al. [Park 2010a, 2010b]. The planarity achieved with the indirect (hohlraum) drive and the excellent performance of the micro-flag (foil) backlighter have enabled growth factor measurements with error bars less than 20%. The flow stress is inferred from the growth factor using a strength model, as explained in the next subsection, and a 20% uncertainty in the growth factor translates to a ~20% statistical uncertainty in the flow stress. Achieving this level of accuracy enables the determination of the effect of material strength on the hydrodynamics including hydrodynamic instabilities. A rather extensive series of experiments is overplotted, where the grain size of the Ta samples was varied. The Ta initial microstructures studied in these RT experiments corresponded to sputtered samples with columnar grain sizes of ~0.25 μm lateral extent; wrought Ta with grain size of ~10 μm; wrought Ta with larger, ~100 μm grains; [100] single crystal Ta; and [111] single crystal Ta. To within the error bars of the RT measurement technique, there were no observable effects of this grain size variation. In particular, a significantly enhanced strength, and reduced RT growth was not observed for the smaller grain sizes, due to the Hall-Petch effect. [Park 2015] The interpretation given is that at the very high strain rates of this experiment, $d\varepsilon/dt \sim 10^7\ s^{-1}$, the dislocation density (ρ_{disloc}) required to accommodate the plastic deformation is sufficiently high that Taylor (work) hardening, which varies as $(\rho_{disloc})^{1/2}$, dominates the other effects, including effects due to grain size (Hall –Petch).

IX.B. Multiscale Modeling of Strength Experiments

The RT experiments are not a direct measurement of strength, in the sense that it is not possible to take the observed ripple growth and do a simple calculation to determine the flow stress. Instead, the experiment is modeled with a continuum hydrodynamics code that uses a model for the strength (flow stress) of the metal. The ripple growth is greatest near peak pressure when the acceleration of the interface is greatest, but there is some growth at other times and the simulation is able to capture all of the accumulated ripple growth from the beginning to when the backlighter goes off. If the simulated ripple growth agrees with the measurements, the strength model is validated. In practice, several strength models have been used, as shown in Fig. 9b. The simulated ripple growth is greatest with no strength (top curve, blue), since there is no resistance to shear flow to slow the ripple growth. Comparison of this curve with the experimental data in Fig. 9b shows that the high-pressure material strength significantly reduces the RT growth. Simulations using the Steinberg-Guinan model [Steinberg 1980] (second curve from the top, orange) and the Preston-Tonks-Wallace model [Preston 2003] (middle curve, red) predict less growth than with no strength, but still growth that is several sigma too large. The simulations using the Livermore multiscale strength (LMS) model [Barton 2011] agree with the growth factors from the experiment within the error bars (bottom curve, black). Both tantalum [Park 2012, 2015] and vanadium [Park 2010a, 2010b] RT experiments have shown that the strength at high pressure (~100 GPa) and high strain rate ($\sim 10^7\ s^{-1}$) is a factor of 4-8 greater than the yield strength at ambient conditions, and in both cases [Park 2012, Park 2010b] the agreement with the LMS model has been good.

This agreement is remarkable since the LMS model was constructed starting from quantum mechanical first principles with essentially no empirical parameters, and specifically no parameters tuned to strength experiments. The model is a hierarchical multiscale model. It is

constructed at the length scales known to be relevant to plasticity: calculations of the quantum mechanics of the electrons binding atoms together are used to construct effective atom-atom force laws without explicit electrons. The force laws are used in turn to determine the mobility laws dictating how lattice defects (dislocations) move under applied stress, as shown in the lower inset of Fig. 9c. An example of one of these dislocation velocity vs. stress curves is shown in Fig. 9c. The mobility laws are then used to calculate material hardening laws (how the flow stress increases as the material is work hardened and the plastic strain increases) using dislocation dynamics simulations that only track the defect positions with no explicit atoms. The resulting hardening laws and dislocation density limits (see the upper inset to Fig. 9c) are used in a continuum strength model suitable for hydrodynamic simulations, simulations that have no explicit electrons, atoms, or dislocations. There are many approximations made in the construction of the model, but no free parameters are left to tune to the experiment. The resulting agreement is remarkable.

The LMS model relates the flow stress to the temperature, pressure and plastic strain rate. It has dislocation density as a state variable that characterizes the microstructure of the metal. The initial dislocation density is input, and then it evolves in the model at each point in space according to the stresses and thermodynamic conditions. The model is time dependent at short time scales, which for Ta is at time scales of a nanosecond or less [Rudd 2012]. It is possible to extract the density and average velocity of the dislocations from hydrodynamic simulations of the RT experiment, as shown in Fig. 9d. As *in-situ* characterization techniques are developed, it may become possible to test these predictions directly with experimental data. It is also possible to decompose the flow stress predictions from the multiscale model into the components (drag, thermal activation, and work hardening), as shown in Fig. 9e for the average conditions of the Ta-RT experiment and simulations shown in Figs. 9b and 9d, resp. Such decompositions motivate potential experiments to test the underlying assumptions of the multiscale model.

IX.C. In-situ Diffraction Strength Experiments

It is possible to determine the flow stress microscopically, at least for single crystal samples. The flow stress is a shear stress, related to local shear strains through the elastic constants: specifically the shear stress is the shear strain times the shear modulus, $\sigma_{shear} = G\varepsilon_{shear}$. X-ray diffraction may be used to probe those shear strains at the level of the unit cell of the crystal lattice of the metal. That is, a metal consists of a regular lattice of atoms. For tantalum and vanadium, each atom is surround by eight nearest neighbors at the corners of a cube. Those cubic unit cells repeat in a regular lattice throughout the sample. The lattice is not perfect; there are point defects (vacancies and interstitials), line defects (dislocations) and other flaws in the crystal. Even in highly defective crystals, however, most of the atoms are surrounded by a cube of nearest neighbors, and that cube is only slightly distorted. The distortion is the shear strain at that point, and it may be probed using x-ray diffraction.

In-situ broadband Laue x-ray diffraction experiments have been carried out on shocked Ta foils at the Omega laser in Rochester [Comley 2013], as shown in Fig. 10a. The shock pressures ranged from 35 to 180 GPa (0.35 to 1.8 Mbar). Broadband Laue diffraction is only sensitive to shear strains in the crystal. Simultaneous VISAR measurements allow the applied longitudinal stress to be measured. With the Laue diffraction measurements, this allows shear strain to be measured vs. shock stress. The diffraction peaks are focused into individual spots on the image plate detector. Hydrostatic compression would leave the spots unshifted from their ambient positions. On the other hand, shear strain shifts the positions of the spots, as shown in Fig. 10a. Measuring that shift gives the shear strain ε_s and, if the shear modulus G is known, the shear stress (flow stress) $\sigma_{shear} \sim G\varepsilon_{shear}$ can be deduced, as shown in Fig. 10b. In the shocked Ta experiments, the shear stress

was found to vary from ~10 GPa to ~35 GPa as the pressure was increased from 35 to 180 GPa (0.35 to 1.8 Mbar). These strength values are high, in agreement with the LMS model extended to include shock heating and to account for homogeneous nucleation of dislocations at the high strain rates at the shock front. [Comley 2013]

IX.D. Ramp Compression/Release Strength Experiments

Another approach to determining the strength of metals at high pressure has been developed by Asay et al. [Asay 2009] and Brown et al. [Brown 2014], and used at the Z machine, a pulsed power facility, to determine the strength of Ta in the pressures up to 250 GPa (2.5 Mbar). Here the samples are typically somewhat larger and the strain rates $\dot{\varepsilon}$ somewhat lower than in the laser experiments: samples 900-2000 microns thick vs. 30-50 microns thick, and $\dot{\varepsilon}$ ~10^5-10^6/s vs. ~10^6-10^7/s for the laser. Magnetic loading was used to take the samples up to the pressure of interest in either the co-axial configuration or the stripline configuration shown in Fig. 11a. In either case a time-varying magnetic field interacts with the current running through the anode on which the samples are mounted, inducing a Lorentz force. The variation in time of the magnetic field is designed to drive a wave that ramps the pressure to a peak and then release it gradually. VISAR was used to measure the resulting surface velocities for both drive measurements and strength measurements in the same shot.

The principle of the experiment introduced by Asay and Lipkin [Asay 1978] is to calculate the shear stress from the Lagrangian sound speeds as the longitudinal stress peaks and releases during which time the material behaves elastically. As the pressure is ramped up the material yields, and the shear stress in the plane-fronted wave is pinned to the yield surface. As the stress peaks and begins to decrease, the shear stress drops inside the yield surface so the response is elastic and eventually goes sufficiently negative to hit the other side of the yield surface. With a number of common assumptions such as simple wave behavior, it is possible to determine the Lagrangian sound speed at points inside the sample from surface velocity (VISAR) measurements. Those Lagrangian sound speeds are then used to determine the change in shear stress crossing the yield surface and thus provide an approximation to the flow stress on loading [Brown 2014].

The longitudinal stress vs. strain curves from a series of experiments loading Ta from 60 to 250 GPa (0.6 to 2.5 Mbar) were measured, along with a curve generated from the SESAME 90210 equation of state. The inferred flow stress Y vs. pressure is plotted in Fig. 11b, along with the results from other experiments. These other experiments were not necessarily at the same temperature, strain rate or total strain. As seen in the figure, the Ta flow stress measurements generally agree with earlier dynamic measurements and the SG and PTW models at pressures below 60 GPa (0.6 Mbar), but become stiffer than those models at higher pressures. The LMS model provides the closest approximation at higher pressures, but it too underestimates the strength. The data follow different trends according to the batch of material, which is attributed to a dependence of the flow stress on the initial microstructure, an observation which differs from that of the laser driven Ta Rayleigh-Taylor strength experiment at higher strain rates, shown in Fig. 9.

X. Shock Vaporization of Silica

Understanding shock-induced melting and vaporization is important for developing realistic models of planetary formation dynamics. [Kraus 2012] In particular, it is thought that the formation of planets and planetary systems involves energetic collisions between planets and planetessimals. For example, the last giant impact is thought to explain the diverse characteristics of the planets in the Solar System [Stewart 2012], including the large core of Mercury [Benz

1988, 2007], formation of Earth's moon [Canup 2001], and Pluto's moons [Canup, 2005]. These collisions attain shock pressures that result in significant levels of melting and vaporization. Yet accurate understanding of shock-induced melting and vaporization for planetary constituent materials is lacking. Planetary collisions are particularly challenging to model because of the need to understand both the extreme temperatures and high compression ratios achieved in the shocked states and the low densities and temperatures of the shock-vaporized material on release. Experiments are required to constrain the equation of state throughout the phase space traversed in modeling these planetary impact and release impact dynamics.

The irreversible work from shock compression can be dissipated as heat through an increase in either temperature or entropy, where the balance between temperature and entropy depends upon the heat capacity. One of the methods used in the planetary community for predicting the amount of melting and vaporization that occurs during planetary impact events (as well as in strong shock and release experiments in the laboratory) is the so-called "Entropy Method". [Ahrens 1972] The technique assumes that a strong shock upon breaking out through a free surface will release into vacuum along an isentrope. Since the leading edge of the releasing material is at ambient pressures, standard laboratory experiments can establish the entropy there, for a given temperature. Then if the release dynamics, namely, density and temperature as a function of the distance of release, can be determined, one can use the isentropic release to set the entropy behind the shock prior to shock break out. [Kraus 2012]

The experimental configurations used at the Janus laser for these shock entropy experiments in silica are shown in Fig. 12a. In a configuration similar to this, but without the LiF window, experiments measured the shock strength as the shock traverses the quartz sample, and gave the shock strength and temperature at shock breakout from the quartz free surface. The diagnostics were a streaked line VISAR and a streaked optical pyrometer (SOP). [Kraus 2012] These experiments were followed with experiments where the shocked quartz released across a known vacuum gap thickness, then stagnated on a LiF window, which is the configuration shown in Fig. 12a. Since the shocked quartz releases as a liquid-vapor mixture, its density drops monotonically as this mixture releases across the gap until it stagnates and accumulates on the LiF window. The result is a ramped compression wave moving into the LiF window. The gap size and shock strength were varied in a series of experiments, and the temperature and density of the releasing SiO_2 mixture of liquid and vapor was determined.

The combined analysis of these two variations of the Janus experiments allowed the experimental temperature-entropy plot to be created, as shown in Fig. 12b. To interpret the observed post-shock temperatures, a model was developed for the apparent temperature of a material isentropically decompressing through the liquid-vapor coexistence region. Using published thermodynamic data, the liquid-vapor boundary for silica was modified based on these experiments and finally the entropy on the quartz Hugoniot was calculated, shown by the open circle plotting symbols. Note the shape of the liquid-vapor curve in Fig. 12b (the gray continuous curve with a peak at entropy of ~5000 J/kg/K). At the highest entropies (strongest shock strength), the temperature of the releasing, co-existing liquid-vapor SiO_2 is dropping, due to an increase in the fraction of liquid that has vaporized (and the internal energy absorbed due to the latent heat of vaporization). At the lowest shock strengths in the quartz, the temperature of the releasing SiO_2 is lower, due to the lower internal energy deposited into the quartz from the weaker shock. This leads to the peaked T-S shape often referred to as the "vapor dome".

The impact of these experiments are revised critical shock pressures for vaporization which are lower than previously estimated, primarily due to the revised entropy on the quartz Hugoniot. As the thermodynamics of other silicates are expected to be similar to quartz, it is concluded that

vaporization is a significant process during high-velocity planetary collisions. For a given shock strength, a higher fraction of vaporization is expected upon release, using the adjusted liquid-vapor boundary resulting from these experiments.

XI. Ramp Compression of Carbon to 5 TPa

Recently experiments have been developed using the ~2 MJ National Ignition Facility (NIF) laser at LLNL to study the properties of matter at many tens of megabar pressures. The first of these experiments used the very precise laser pulse shaping capability of the NIF laser, which was developed partly to drive ICF capsule implosions to very high densities for fusion energy research. The same type of pulse shaping for the 192 NIF lasers focused into a standard NIF ICF radiation cavity ("hohlraum") was refined to drive a planar diamond (carbon) target mounted on the wall of the hohlraum (as opposed to a spherical capsule located at the center of the hohlraum), to probe the very high pressures relevant to planetary and brown dwarf interiors. [Smith 2014] The theoretical description of such electron-degenerate matter has recently suggested that new complexities can emerge at pressures where core electrons (not only valence electrons) influence the structure and bonding of matter. This new experimental work describes ramp-compression measurements for diamond, reaching nearly 4-fold compression at a peak pressure of 5 terapascals (50 Mbar). These data can now be compared to first-principles density functional calculations and theories long used to describe matter present in the interiors of giant planets, in stars, and in inertial-confinement fusion experiments. These data also provide new constraints on mass–radius relationships for carbon-rich planets. [Swift 2012]

The experimental configuration used for these high-pressure ramp compression experiments on NIF is shown in the inset of Fig. 13a. A highly shaped laser pulse is generated by focusing 176 synchronized, 20 ns duration laser beams into a hollow cylindrical Au radiation cavity, called a hohlraum, converting to a temporally shaped radiation temperature, $T_r(t)$ vs. time. A hole is cut into the side of the hohlraum wall, and a planar physics package, consisting of a 50 μm synthetic diamond ablator, a 10 μm Au x-ray preheat shield, and 4 precision steps of synthetic diamond, is mounted over this hole. The shaped radiation drive launches a ramped compression wave through these diamond steps, and the free surface velocity vs. time, $u_{fs}(t)$, is measured as the waves break out of the back side using a streaked line VISAR diagnostic, as shown in Fig. 13a. The free surface velocity profiles shown in Fig. 13a are analyzed by an iterative Lagrangian method developed by Rothman,[Rothman 2005], to generate the stress-density results for carbon shown in Fig. 13b. For reference, the pressures at the center of Earth, Neptune, and Saturn are indicated on the vertical axis by the red arrows.

This stress-density result for carbon, which is thought to remain solid throughout the ramped compression wave, can be compared with the results of a number of equations of state (EOS) models in the multi-terapascal regime. Comparisons to a density functional theory (DFT) calculated cold curve, and a DFT Hugoniot curve are shown by the dashed and solid red curves, respectively. These two curves, based on quantum mechanical theory and taking into account the lattice structure of the carbon, bracket the experimental data on either side. The DFT Hugoniot predicts the carbon to be liquid at the higher stresses (> ~1 TPa), and less compressible than observed. The DFT cold curve, however, predicts the carbon to be more compressible than observed, and also predicts two phase transitions, which appear as stress plateau kinks in the otherwise smoothly rising stress-density curves: diamond to BC8 at ~0.99 TPa and BC8 to simple cubic at ~2.7 TPa. Neither of these two kinks is apparent in the experimental data, which remains very smooth throughout the compression. It may be that kinetic effects due to the high rates of compression smooth out these phase transition kinks. Or it may be that, due to the short time scales of the experiments, the phase transitions have not yet had time to complete themselves.

Additional experiments on NIF continue to explore the high-pressure properties of carbon. What is clear is that the experimental data are less compressible than the DFT cold curve, more compressible than the DFT Hugoniot, and do not show the traditional stress-density discontinuities (plateau kinks) typically seen from phase transitions. The peak stresses achieved exceed those at the centers of Earth (360 GPa), Neptune (~800 GPa), and Saturn (~4 TPa), thus opening up a new capability of probing material properties at conditions matching the deep interiors of giant planets. [Smith 2014].

XII. Material properties at 100 TPa (1 Gbar)

To study the properties of matter at the highest pressures (~100 TPa or 1 Gbar) and densities requires spherical convergence. We describe a NIF experiment under development to probe matter, and measure the equation of state, in a shocked converging solid sphere of low-Z material. The materials being studied in this development project are CH, CD, and diamond (carbon). A schematic of the experimental setup is illustrated in Fig. 14a. [Kritcher 2014] Here solid targets of CH or CD are shock compressed using a hohlraum radiation source. The plasma is probed with x-ray radiography in the equatorial direction and x-ray scattering in the polar direction. A wedged cross-section of the solid CH target with a Ge doped CH ablator is shown on the upper left, giving the radii of the layers, and the percent dopant of the Ge layers. The Ge layers are to block the M-band hard x-rays from the hohlraum drive from preheating the solid CH sphere that is being shock compressed.

The experiments and data analysis are still in progress. The design point being pursued, however, is illustrated with the pressure – radius plot shown from the design simulations in Fig. 14b. [Kritcher 2014] Pressure as a function of shock radius are given for simulations using equation of state LEOS 5350 (red), LEOS 5400 (green), and Sesame 7592 (black). Note that to reach pressures of ~1 Gbar require convergences down to radii < 100 μm. The inset of Fig. 14b shows a simulated radiograph for 9 keV x-rays as a function of time and capsule radius. Here, the integrated transmission is convoluted with the backlighter function in time and space. Also plotted is the location of the predicted self-emission flash. Fiducial wires are used to determine the magnification of the instrument and a 4ω fiducial is used to determine the absolute diagnostic timing. The challenges posed by measurements at these maximal convergences are (1) the finite spatial and temporal resolutions of the diagnostics start to have a significant impact; (2) the self emission flash may potentially start to be a source of background; and (3) at the highest convergences and pressures, the Ge preheat shield layers have been burned through, so now the CH sample being studied is at risk of being preheated by the hard x-ray component of the drive.

XIII. Conclusion

With modern high energy density (HED) experimental facilities, such as high-power, high-energy lasers, pulse power magnetic pinch facilities, and advanced light sources coupled with capabilities to launch shock waves into samples, matter can now be studied experimentally with precision at very high pressures and over very short time scales. Laboratory studies can now be conducted on the basic properties of matter, such as phase, strength, conductivity, and ductility at conditions matching those of planetary interiors, including the now more than 1000 discovered exoplanets. [Schneider 2011; Seager 2007] Furthermore, the time response to matter as it is being compressed can now be measured down to sub-picosecond resolution, and over micron spatial scales. For the first time, this allows quantitative direct one-to-one comparisons of experimental data with molecular dynamics simulations, whose interatomic potential is tied to quantum mechanics. Also,

new multiscale theoretical models now can simulate macroscopic material response with information passing methodologies that allow direction connection back to quantum based interatomic potentials. With these modern experimental and theoretical capabilities, the pace of new discoveries in the properties, phases, and states of matter is accelerating, which highlights one of the most exciting eras in science. And in particular, coupled with the studies of planetary formation, the formation of planetary systems, and investigations of the likely environments in, on, and around the exoplanets, these new experimental and theoretical capabilities are tied to far reaching explorations about the universe.

Figure Captions

Figure 1. (a) Iron (Fe) phase diagram up to Earth inner core conditions (dashed red box). There are uncertainties associated with the melting curve above 100 GPa as well as possible additional solid phases at very high pressures. The orange shaded region shows a range of possible temperatures for the Earth's interior. The pressure-depth scale is obtained from the seismic Preliminary Reference Earth Model. [Dziewonski 1981] The Hugoniot (purple curve) crosses the melting curve at ~225-243 GPa. The blue curve shows the temperature rise associated with compression along the principal isentrope, which serves as a lower bound to the temperature achieved in ramp loading from ambient conditions as additional heating due to plastic work is expected. Possible experimental paths showing an initial shock followed by isentropic compression (green and red curves) are also shown. The temperature estimates were obtained from the Hugoniot temperature achieved in the initial shock and by the temperature rise due to isentropic compression. Reproduced from [Wang 2013]. (b) Free surface velocity history measurement for shocked iron in a powder gun driven plate impact experiment, at peak shock stress of 23.7 GPa. Reproduced from [Barker 1974] (c) Free-surface velocity versus time measurements from a ramp wave, uniaxial loading experiment on iron at the Sandia Z-machine. The inset shows the time-dependent decay of the velocity plateau associated with the $\alpha - \varepsilon$ phase transformation. Reproduced from [Smith 2013]. (d) A compendium of experiments using ramp wave compression of iron, and plotting the α–ε transition stress as a function of strain rate associated with the phase transition, $(d\mu/dt)_{\alpha-\varepsilon}$. Inset: Peak elastic stress versus strain-rate at the onset of plastic flow in Fe. The data of Crowhurst and Armstrong was obtained on ~1 μm thick Fe samples driven with a 50 μJ, ~270 ps, 800 nm wavelength short pulse, Ti:sapphire table-top laser. [Crowhurst 2014] The different plotting symbols correspond to different experimental conditions and facilities, as described in [Smith 2013]. Adapted from [Smith 2013].

Figure 2. (a) The experimental setup for a dynamic diffraction experiment showing schematically the x-ray diffraction signal from the (1) unshocked and (2) shocked single crystal Si. (b) Diffraction results from unshocked and shocked Si where the 6.7 GPa (67 kbar) shock propagation direction was along the Si [111], and the streaked (time-resolved) diffraction was from the (111) lattice planes. Reproduced from [Wark 1987].

Figure 3. (a) A schematic of the experimental setup (center), along with time integrated transmission Bragg diffraction from (040) Si lattice planes (left side) and reflection Bragg diffraction from (400) Si lattice planes (right side). (b) Time-resolved x-ray streak camera image of the reflection Bragg diffraction signal shown in Fig. 1a. The diffraction angle and corresponding compression of the (400) lattice are shown as a function of time with respect to the start of the drive laser. (c) Profiles of the time-integrated Bragg diffraction signals from shocked single-crystal Si in the reflection (400) geometry, and (d) in the transmission (040) geometry. In (c) and (d), the upper traces correspond to the shot shown in (a) and (b), with a peak compression

of 6.2%, the middle traces for a shot with similar peak compression, but slightly different drive history, and the lower traces for a shot with peak compression of 11%. Reproduced from [Loveridge-Smith 2001].

Figure 4. (a) Dislocation structure resulting from molecular dynamics (MD) simulations of shocked [100] copper. A snapshot of a simulation with a 50 ps linear-ramp rise time, shown after t ~ 100 ps, showing only dislocation atoms. The copper crystal included pre-existing dislocation sources. The color is only to enhance the view of the dislocations. The three regions of dislocation activity—homogeneous, mixed and multiplication—are marked. Adapted from [Bringa 2006]. (b) Response of the MD lattice during 3D plastic relaxation. The relaxation of the shear stress from simulated X-ray diffraction, as a function of time behind the shock front. The black horizontal dashed line indicates the value for full 3D relaxed compression. The red curve corresponds to the 0 ps rise-time shock case, and the blue curves to the 50-ps ramped case. Adapted from [Bringa 2006]. (c) Experimental configuration for the LCLS experiment measuring the shock response of a 1 μm thick shocked Cu polycrystalline sample with a preferential [111] orientation. The lattice response was captured in a Debye-Scherrer geometry by a series of 48-fs snapshots. (d) Simulated diffraction profiles, which were in good agreement with experiment, show the evolution of the lattice response in 20 ps steps from the unshocked lattice to the elastic precursor compression, and the plastic relaxation of the compressed lattice. Adapted from [Milathianaki 2013] (e) Calculated elastic and plastic strain vs. time at a sample depth of 200 nm. Note that the plastic relaxation (plastic strain) does not begin until the normal elastic strain reaches a peak value of ~18%. Reproduced from [Milathianaki 2013]. (f) Stress-strain curves from MD simulations of shocked Cu along the [123], [110], and [111] directions (left vertical scale), and [001] (right vertical scale) at 300 K and strain rate of 10^8 s^{-1}. The strain threshold for dislocation nucleation (onset of plasticity) is indicated with arrows. [Reproduced from [Dupont 2012]

Figure 5. (a) Sample image of the diffraction data from reflection for shocked single crystal iron for a 26 GPa (260 kbar) shock in the [001] direction. Diffraction from the static bcc lattice is shown in blue, from the elastically compressed bcc lattice in green, and from the hcp phase in red. (b) Volume of the compressed iron plotted vs peak drive pressure. Solid points represent the peak compression observed, and open points represent the lower compression observed for each experiment. Results from postprocessed MD simulations (black circles), and the room temperature shock Hugoniot (gray curve) are shown overlaid. Reproduced from [Kalantar 2005]. (c) MD simulation of shocked iron (shock fronts propagate from left to right) after 8.76 ps in the bcc [001] direction for a shock strength of 471 m/s (u_p = 471 m/s, u_p/c_0 = 0.0951, P_{shk} ~ 15 GPa). Atoms are color-coded by the number of neighbors n within 2.75 Å. Gray, unshocked bcc (n = 8); blue, uniaxially compressed bcc (n = 10); and red, the transformed close-packed grains (n = 12) separated by yellow (n = 11) grain boundaries. This shock strength is just above the α–ε transformation threshold. (d) Nucleation of close-packed (hcp) material in the shocked [001] Fe at P_{shk} ~ 15 GPa, which is just above the α–ε transformation threshold. Only atoms with a transverse movement above 0.42 Å are shown and colored by their transverse displacement [gray = 0.42 Å, cyan = 1.32 Å (about half the nearest neighbor distance)]. After 1.095 ps (left), small nucleation centers start to grow along close-packed planes and finally build the transformation front (right, after 2.19 ps). Reproduced from [Kadau 2002]

Figure 6. (a) Experimental set-up for powder X-ray diffraction from ramp-compressed MgO samples at hiogher pressure at the Omega Laser Facility, showing the diagnostic box containing image plates and target assembly sitting in the front plate. X-rays generated by laser illumination

of a Cu foil hit the bottom plate and the diffracted signal is recorded on the other panels (red lines indicate example diffraction at $2\theta = 55^{\circ}$). Additional lasers compress the target, and VISAR measurements allow a pressure determination. (b) Comparison of measured d-spacings in diffraction from the ramp compressed MgO on Omega (gray solid circle plotting symbols) with diamond anvil cell (DAC) experiments (black and red curves) and simulations (dashed blue and dot-dash black curves) below and above 563 GPa for B1 and B2 phase MgO. Reproduced from [Coppari 2013].

Figure 7. (a) Schematic of the experimental configuration for dynamic EXAFS measurements for shocked vanadium and titanium on the principle Hugoniot. The imploding spherical target serves as a continuum x-ray backlighter "point" source for the EXAFS measurements. The three-stacked 3ω laser beams launch a shock through the 10 μm sample tamped on both sides with 17 μm of CH. (b) Fitting the measured V EXAFS spectra for the shocked V experiment with the FEFF8 code. Reproduced from [Yaakobi 2004b]. (c) Experimental EXAFS results for unshocked and shocked iron. The disappearance of the peak marked "w" is a signature of the α to ε phase transformation. Reproduced from [Yaakobi 2005a].

Figure 8. (a) Schematic of the experimental configuration for dynamic EXAFS measurements on iron for off-Hugoniot staged-shock loading to peak pressures approaching 600 GPa. (b) Temperature inferred from the Debye-Waller factor (DWF) in the dynamic EXAFS data for Fe as a function of stress for the staged shock drive with an initial shock of ~150 GPa followed by ramp compression waves up to 570 GPa. The single-shock data are also shown (blue diamonds). The melting curve (dot-dot-dashed lines) and the Hugoniot (green solid lines with dots) are plotted for comparison. Also shown are isentrope curves following the 150 GPa shock for the no-strength case (solid black curve), for a calculation assuming strength based on static data, Y_{sta} (dotted lines), and for a calculation assuming "dynamic strength" is a factor of 3 greater than static strength, $Y_{dyn} = 3Y_{sta}$ (dashed lines). Including Fe strength in the analysis increases the temperature due to the work done against strength in compressing the Fe sample. Reproduced from [Ping 2013].

Figure 9. (a) Schematic of the experimental setup to infer Ta flow stress (strength) at high pressure and high strain rate at the Omega laser facility, using the Rayleigh-Taylor instability. [Park 2015] Radiation from the hohlraum drives the reservoir/gap configuration (not to scale) creating a ramped plasma drive that compresses and accelerates the sample material without shock melting. Reproduced from [Park 2015]. (b) Time histories of simulation results for laser-driven Rayleigh–Taylor instability growth in the solid-state, plastic flow regime of tantalum, at peak pressures of ~100 GPa. The predicted growth factor vs. time for various strength models is shown, as well as an extensive set of experimental data from the Omega laser. Reproduced from [Park 2015]. (c) Molecular dynamics simulation results (points) and calibrated functional forms (smooth curves) for the mobility of screw dislocations in tantalum at zero pressure. Upper inset: Saturation dislocation density as a function of plastic strain rate for tantalum from dislocation dynamics simulations and a power-law fit to the results. Adapted from [Park 2015]. Lower inset: Screw dislocation in Ta under high stress leaving interstitial and vacancy debris in its wake. Only those atoms at defective lattice sites are shown. The dislocation core is the line of red atoms. The colors just indicate position: the dislocation is moving on a glide plane from blue to red (right to left). Adapted from [Rudd SCCM 2014]. (d) Spatial distribution of quantities in the tantalum for a laser-driven Rayleigh–Taylor instability growth simulation at roughly 50 ns. The other materials in the simulation are not shown. Dislocation density (lower plot) is plotted with a logarithmic scale, and dislocation velocity (upper plot) is on a linear scale. Adapted from [Barton 2011]. (e) Decomposition of the Ta multiscale strength model results for parameters

corresponding to the simulation shown in (d): P = 1 Mbar and T=1270 K.

Figure 10. (a) Experimental configuration. The crystal sample is mounted on a pinhole on the front of the shielded diagnostic box which is lined with image plate detectors. The Ta single crystal sample is shock-loaded along the [100] direction using a single beam of the OMEGA laser system. The VISAR axis for simultaneously measuring the drive is aligned along the [100] direction. Continuum (white light) x rays from a capsule implosion driven by 44 beams are collimated by the pinhole and diffracted from the sample to produce a characteristic Laue diffraction pattern on image plate detectors mounted on the interior of the BBXRD enclosure. Each diffraction spot corresponds to diffraction from a particular crystallographic plane and is formed by the quasicollimating effect of the pinhole on which the crystal sample is mounted. (b) Flow stress (strength) vs. pressure as determined from the experiment, in comparison to strength predicted by the Steinberg-Guinan (SG), Steinberg-Lund (SL), Preston-Tonks-Wallace (PTW), and the LLNL multiscale (MS) strength models. Inset: effective shear modulus C' vs. pressure P, as calculated from density-functional theory including shock heating on the Hugoniot. Reproduced from [Comley 2013].

Figure 11. (a) Co-axial (left) and stripline (right) load configurations on the SNLA Z high-energy magnetic pinch facility. The coaxial target contains drive measurements on the top and bottom of each anode panel with a sample measurement in between. The stripline target contains three drive measurements on the cathode directly opposed by sample measurements on the anode. (b) Compendium of data sets for Ta over-plotted, along with model simulations of flow stress vs. pressure. The references are given in the legend, along with the type of experiment, characteristic strain rate, and a parenthetical note referring to the type of Ta tested. Reproduced from [Brown 2014].

Figure 12. (a) Schematic target design to experimentally infer entropy on the principle Hugoniot as a function of temperature for shocked quartz, based on a shock-and-release technique. A quasi-steady shock wave is generated by laser ablation of the aluminized sample. Upon shock breakout at the down-range free surface, the released material propagates across the gap and stagnates against an aluminized LiF window. The particle velocity in the LiF and time of impact were measured for three gap distances after 199 and 338 GPa shocks in the quartz sample. (b) Post-shock temperatures (filled circles) based on streaked optical pyrometry (SOP) measurements for quartz [Boslough, 1988; Kraus 2012] and fused silica [Boslough, 1988] compared to revised model liquid-vapor phase boundary from this study. The Hugoniot states achieved in each shock-and-release experiment (open circles) are placed at the entropy and temperature corresponding to the measured shock velocity. Reported uncertainties in entropy reflect both uncertainties in the experimental shock pressure and the absolute entropy on the Hugoniot. [Reproduced from Kraus 2012]

Figure 13. Velocity interferometry for ramp compressed diamond to ~5 TPa (50 Mbar) peak pressures on the NIF laser. (a) The free-surface velocity u_{fs} versus time from the back of the diamond steps obtained from VISAR. The target (inset) consists of a gold cylindrical radiation cavity (hohlraum) within which the 351-nm- wavelength laser light is converted to an X-ray flux that is absorbed by the diamond sample attached to the side of the hohlraum. The X-rays ablate and ramp-compress the sample, and the free-surface velocity is recorded for four thicknesses (steps) of diamond: 140.0 mm (red line), 151.7 mm (blue line), 162.6 mm (black line) and 172.5 mm (green line). (b) The free surface velocity vs. time through the 4 steps of diamond are analyzed to produce longitudinal stress versus density. Model comparisons include simulated

Hugoniots based on density functional theory (DFT) (solid red line) and a Mie–Gruneisen EOS (solid orange line); cold curves from DFT (red dashed line), statistical-atom models (Thomas-Fermi, Thomas-Fermi-Dirac, TFD-W and TFD-Wc as green dotted, short dashed, long dashed and solid lines), and Vinet (gray dot-dashed line) and Birch–Murnaghan (grey dashed line) EOS fits to static data. Static diamond anvil cell (DAC) data are shown as the green circles in the lower left corner. Shaded regions between cold curves (gray) or Hugoniot curves (orange) show roughly the range of uncertainty in the EOS in this terapascal regime. The pressures at the center of Earth, Neptune and Saturn are shown with red arrows along the vertical axis for reference. The inset highlights the differences in the models at low pressure. Reproduced from [Smith 2014].

Fig. 14. (a) Schematic of the experimental setup for radiography measurements of EOS at near-Gbar pressures. Here solid targets of CH, CD, or diamond (carbon) are shock compressed using a hohlraum radiation source. The plasma is probed with x-ray radiography in the horizontal direction and x-ray scattering in the polar direction. The inset at the upper left shows a wedged cross-section of the solid CH target with a Ge doped CH ablator. Shown on the left hand side are the radii of the layers, and on the right hand side are the percent dopant of the Ge layers. (b) Pressure as a function of shock radius for simulations using various equation of state models: LEOS 5350 (red), LEOS 5400 (green), and Sesame 7592 (black). Inset: Simulated radiograph of an imploding solid CH sphere, with a noise function derived from previous shots. Also plotted is the location of the predicted self-emission flash. Fiducial wires are used to determine the magnification of the instrument and a 4ω fiducial is used to determine the absolute diagnostic timing.

References:

*This work performed under the auspices of the U.S. Department of Energy by Lawrence Livermore National Laboratory under Contract DE-AC52-07NA27344.

[Ahrens 1972] Ahrens, T. J., and J. D. O'Keefe, "Shock melting and vaporization of lunar rocks and minerals," Moon, 4(1–2), 214–249 (1972).

[Asay 1978] J.R. Asay and J. Lipkin, JAP 49, 4242 (1978).

[Asay 2009] J. R. Asay, T. Ao, T. J. Vogler, J. P. Davis, and G. T. Gray, J. Appl. Phys. **106**, 073515 (2009).

[Bancroft 1956] Dennison Bancroft et al., J. Appl. Phys. 27, 291 (1956).

[Barker 1974] L.M. Barker and R.E. Hollenbach, JAP 45, 4872 (1974).

[Barnes 1974] John F. Barnes et al., J. Appl. Phys. 45, 727 (1974).

[Barton 2011] N.R. Barton et al., JAP 109, 073501 (2011).

[Barton 2013] Nathan Barton and Moon Rhee, JAP 114,123507 (2013).

[Behr 2000] J. Rehr and R.C. Albers, *Rev. Mod. Phys.*, 2000, **72**, 621.

[Belof 2012] Jonathan Belof et al., proceedings, APS-SCCM-2011 (2012).

[Benuzzi-Mounaix 2014] Alessandra Benuzzi-Mounaix, Phys. Scr. T161, 014060 (2014).

[Benz 1988] Benz, W., W. L. Slattery, and A. G. W. Cameron, Collisional stripping of Mercury's mantle, Icarus, 74(3), 516–528 (1988).

[Benz 2007] Benz, W., A. Anic, J. Horner, and J. A. Whitby, The origin of Mercury, Solar Syst. Rev., 132, 189–202 (2007).

[Boehly 1997] T. R. Boehly *et al.*, Opt. Commun. **133**, 495 (1997).

[Boslough 1988] Boslough, M. B., "Postshock temperatures in silica," J. Geophys. Res., 93(B6), 6477–6484 (1988).

[Bringa 2006] E.M. Bringa et al., Nature Materials 5, 805 (2006).

[Brown 2014] J.L. Brown et al., JAP 115, 043530 (2014).

[Buffett 2000] B.A. Buffett, Science 288, 2007 (2000).

[Canup 2001] Canup, R. M., and E. Asphaug, Origin of the moon in a giant impact near the end of the Earth's formation, Nature, 412(6848), 708–712 (2001).

[Canup, 2005] Canup, R. M., A giant impact origin of Pluto-Charon, Science 307, 546–550 (2005).

[Colvin 2003] J.D. Colvin et al., J. Appl. Phys. 93, 5287 (2003).

[Comley 2013] A. J. Comley, B. R. Maddox, R. E. Rudd, S. T. Prisbrey, J. A. Hawreliak,1 D. A. Orlikowski, S. C. Peterson, J. H. Satcher, A. J. Elsholz, H.-S. Park, B. A. Remington, N. Bazin, J. M. Foster, P. Graham, N. Park, P. A. Rosen, S. R. Rothman, A. Higginbotham, M. Suggit, and J. S. Wark, Phys. Rev. Lett. **110**, 115501 (2013).

[Coppari 2013] Frederica Coppari et al., Nature Geoscience 6, 926 (2013).

[Comley 2013] Andrew Comley, PRL 110, 115501 (2013).

[Crowhurst 2011] Jonathan C. Crowhurst et al., PRL, 107, 144302 (2011).

[Crowhurst 2014] Jonathan C. Crowhurst et al., JAP 115, 113506 (2014).

[Denoeud 2014] A. Denoeud et al, PRL 113, 116404 (2014).

[Di Cicco 1994] A. Di Cicco et al., Phys. Rev. B 50, 12386 (1994).

[Ding 2007] Y. Ding et al., Phys. Rev. Lett. 98, 085502 (2007).

[Dubrovinsky 2012] L. Dubrovinsky et al., Nat. Commun. 3, 1163 (2012).

[Dupont 2012] Virginie Dupont and Timothy C. Germann, PRB 86, 134111 (2012).

[Dziewonski 1981] A. M. Dziewonski and D. L. Anderson, Phys. Earth Planet. Inter. 25, 297

(1981).

[Edwards 2011] M.J. Edwards et al., Phys. Plasmas 18, 051003 (2011).

[Edwards 2013] M.J. Edwards et al., Phys. Plasmas 20, 070501 (2013).

[Fortney 2009] J. J. Fortney, S. H. Glenzer, M. Koenig, B. Militzer, D. Saumon, and D. Valencia, Phys. Plasmas 16, 041003 (2009).

[Haan 2011] S.W. Haan et al., Phys. Plasmas 18, 051001 (2011).

[Hawreliak 2006] J. Hawreliak et al., PRB 74, 184107 (2006).

[Hawreliak 2008] J. Hawreliak et al., PRB 78, 22010 (R) (2008).

[Hawreliak 2011] J. Hawreliak et al., Phys. Rev. B 83, 144114 (2011).

[Hemley 1997] Russell J. Hemley et al., Science 276, 1242 (1997).

[Higginbotham 2009] A. Higginbotham et al., High Energy Density Phys. 5, 44 (2009).

[Holian 1998] B.L. Holian and P.S. Lombdahl, Science 280, 2085 (1998).

[Kadau 2002] Kai Kadau, Timothy C. Germann, Peter S. Lomdahl, and Brad Lee Holian, Science **296**, 1681 (2002).

[Kadau 2007] K. Kadau et al., Phys. Rev. Lett. 98, 135701 (2007).

[Kalantar 2005] D.H. Kalantar et al., PRL 95, 075502 (2005).

[Konningsberger 1988] D.C. Konningsberger and R. Prins, *X-ray Absorption: Principles, Applications, Techniques of EXAFS, SEXAFS, and XANES* (John Wiley & Sons, 1988).

[Kraus 2012] R. G. Kraus, S. T. Stewart et al., JGR 117, E09009 (2012).

[Kritcher 2011] A.L. Kritcher et al., Phys. Rev. Lett. 107, 015002 (2011).

[Kritcher 2014] A.L. Kritcher et al., HEDP 10, 27 (2014).

[Lee 1981] P.A. Lee, P.H. Citrin, P. Eisenberger, and B.M. Kincaid, *Rev. Mod. Phys.* **53**, 769 (1981).

[Loveride-Smith 2001] A. Loveridge-Smith et al., Phys. Rev. Lett. 86, 2349 (2001).

[Ma 2013] T. Ma et al., Phys. Rev. Lett. 111, 085004 (2013).

[Matzen 2005] M. Keith Matzen et al., Phys. Plasmas 12, 055503 (2005).

[McWilliams 2012] R. Stewart McWilliams, Dylan K. Spaulding, Jon H. Eggert, Peter M. Celliers, Damien G. Hicks, Raymond F. Smith, Gilbert W. Collins, Raymond Jeanloz, Science 338, 1330 (2012).

[Melosh 2007] Melosh, H. J., "A hydrocode equation of state for SiO_2," Meteor. Planet. Sci., 42(12), 2079–2098 (2007).

[Milathianaki 2013] Despina Milathianaki et al., Science 342, 220 (2013).

[Mishin 2001] Y. Mishin et al. Phys. Rev. B 63, 224106–224121 (2001).

[Mogni 2014] G. Mogni, A. Higginbotham, K. Gaál-Nagy, N. Park, and J.S. Wark, Phys. Rev. B 89, 064104 (2014).

[Murphy 2010] W.J. Murphy et al., J.Phys: Cond.Mat. 22, 065404 (2010).

[Nguyen 2004] Jeffrey H. Nguyen et al., Nature 427, 339 (2004).

[Park 2010a] Hye-Sook et al., Phys. Rev. Lett. 104, 135504 (2010).

[Park 2010b] H.-S. Park, B. A. Remington, R. C. Becker, J. V. Bernier, R. M. Cavallo, K. T. Lorenz, S. M. Pollaine, S. T. Prisbrey, R. E. Rudd, and N. R. Barton, Phys. Plasmas **17**, 056314 (2010).

[Park 2015] Hye-Sook Park et al., Phys. Rev. Lett., in press (2015).

[Park 2012] H. S. Park, N. R. Barton, J. L. Belof, K. J. M. Blobaum, R. M. Cavallo, A. J. Comley, B. R. Maddox, M. J. May, S. M. Pollaine, S. T. Prisbrey, B. A. Remington, R. E. Rudd, D. W. Swift, R. J. Wallace, M. J. Wilson, A. Nikroo, and E. Giraldez, in Shock Compression of Condensed Matter— 2011, edited by M. L. Elert, W. T. Buttler, J. P. Borg, J. L. Jordan, and T. J. Vogler (American Institute of Physics, Melville, 2012), Vol. 1426, p. 1371.

[Ping 2013] Yuan Ping et al., PRL 111, 065501 (2013).

[Preston 2003] D. L. Preston, D. L. Tonks, and D. C. Wallace, J. Appl. Phys. **93**, 211 (2003).

[Rehr 2000] J.J. Rehr and R.C. Albers, Rev. Mod. Phys. 72, 621 (2000).

[Remington 1999] Bruce A. Remington et al., Science 284, 1488 (1999).

[Remington 2000] Bruce A. Remington et al., Phys. Plasmas 7, 1641 (2000).

[Remington 2004] B.A. Remington et al., Met. Mat. Trans. A 35A, 2587 (2004).

[Remington 2006a] Bruce A. Remington et al., Rev. Mod. Phys. 78, 755 (2006).

[Remington 2006b] B.A. Remington et al., Mat Sci. Tech. 22, 474 (2006).

[Remington 2012] B.A. Remington et al., in Shock Compression of Condensed Matter— 2011, edited by M. L. Elert, W. T. Buttler, J. P. Borg, J. L. Jordan, and T. J. Vogler (American Institute of Physics, Melville, 2012), Vol. 1426, p. 1375.

[Robinson 1989] A.C. Robinson and J.W. Swegle, J. Appl. Phys. 66, 2859 (1989).

[Rosen 1996] Mordecai D. Rosen, Phys. Plasmas 3, 1803 (1996).

[Rosen 1999] Mordecai D. Rosen, Phys. Plasmas 6, 1690 (1999).

[Rosen 2015] M.D. Rosen et al., Phys. Plasmas, in prep. (2015).

[Rosolankova 2004] K. Rosolankova et al. in "Shock Compression of Condensed Matter-2003" (eds M.D. Furnish, Y.M. Gupta and J.W. Forbes) 1195 (AIP, Melville, New York, 2004).

[Rothman 2005] Rothman, S. D. et al. "Measurement of the principle isentropes of lead and lead-antimony alloy to ~400 kbar by quasi-isentropic compression". J. Phys. D 38, 733–740 (2005).

[Rudd 2010] R.E. Rudd et al., MRS Bulletin 35, 999 (2010).

[Rudd 2012] R. E. Rudd, A. J. Comley, J. Hawreliak, B. Maddox, H.-S. Park, B. A. Remington, in Shock Compression of Condensed Matter— 2011, edited by M. L. Elert, W. T. Buttler, J. P. Borg, J. L. Jordan, and T. J. Vogler (American Institute of Physics, Melville, 2012), Vol. 1426, p. 1379.

[Rudd 2014] R.E. Rudd et al., J. Phys. Conf. Ser. 500, 112055 (2014).

[Sakaiya 2014] Tatsuhiro Sakaiya et al., Earth, Planetary Sci. Lett. 392, 80 (2014).

[Schneider 2011] Schneider, J., Dedieu, C., Le Sidaner, P., Savalle, R. & Zolotukhin, I. Defining and cataloging exoplanets: the exoplanet.eu database. Astron. Astrophys. 532, A79 (2011).

[Seager 2007] Seager, S., Kuchner, M., Hier-Majumder, C. A. & Militzer, B. Mass-radius relationships for solid exoplanets. Astrophys. J. 669, 1279–1297 (2007).

[Sevillano 1979] E. Sevillano, H. Meuth, and J.J. Rehr, Phys. Rev. B 20, 4908 (1979).

[Shigemori 2012] K. Shigemori et al., RSI 83, 10E529 (2012).

[Smith 2008] R.F. Smith et al., PRL 101, 065701 (2008).

[Smith 2013] R.F. Smith et al., JAP 114, 223507 (2013).

[Smith 2014] R.F. Smith et al., Nature 511, 330 (2014).

[Sotin 2007] C. Sotin, O. Grasset, and A. Mocquet, Icarus 191, 337 (2007).

[Steinberg 1980] D. J. Steinberg, S. G. Cochran, and M. W. Guinan, J. Appl. Phys. **51**, 1498 (1980).

[Stenberg 1989] D.J. Steinberg and C.M. Lund: *J. Appl. Phys*,, vol. 65, p. 1528 (1989).

[Stewart 2012] Sarah T. Stewart and Zoe M. Leinhardt, Astrophys. J. 751, 32 (2012).

[Swegle 1989] J.W. Swegle and A.C. Robinson, J. Appl. Phys. 66, 2838 (1989).

[Swift 2012] D. C. Swift, J. H. Eggert, D. G. Hicks, S. Hamel, K. Caspersen, E. Schwegler, G. W. Collins, N. Nettelmann, and G. J. Ackland, Astrophys. J. 744, 59 (2012).

[Valencia 2006] D. Valencia, R. J. O'Connell, and D. Sasselov, Icarus 181, 545 (2006).

[Valencia 2009] D. Valencia, R. O'Connell, and D. Sasselov, Astrophys. Space Sci. 322, 135 (2009).

[Wark 2007] Justin Wark et al., Proc. SCCM-07, p.286 (2007).

[Wark 1987] J.S. Wark et al., Phys. Rev. B., Rapid Commun., 35, 9391 (1987).

[Wark 1989] Justin S. Wark et al., Phys. Rev. B 40, 5705 (1989).

[Wehrenberg 2015] Chris Wehrenberg et al., Phys. Rev. Lett., submitted (2015).

[Yaakobi 2003] B. Yaakobi, F. J. Marshall, T. R. Boehly, R. P. J. Town, and D. D. Meyerhofer, *J. Optical Soc. America B-Optical Physics* **20**, 238 (2003).

[Yaakobi 2004a] B.Yaakobi et al., PRL 92, 095504 (2004).

[Yaakobi 2004b] B.Yaakobi et al., PoP 11, 2688 (2004).

[Yaakobi 2005a] B. Yaakobi et al., PRL 95, 075501 (2005).

[Yaakobi 2005b] Yaakobi, *Phys. Plasmas* **12**, 092703 (2005).

[Zimmerman 1975] G B. Zimmerman and W. L. Kruer, *Comments Plasma Phys. Controlled Fusion* **2**, 51 (1975).

[Zhu 1987] X. Zhu et al., Phys. Rev. B 35, 9085 (1987).

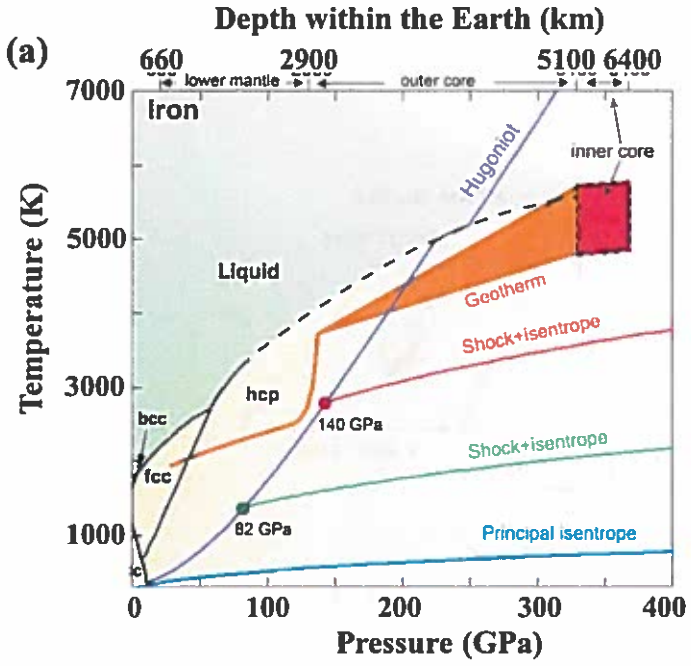

[Jue Wang et al., JAP 114, 023513 (2013)]

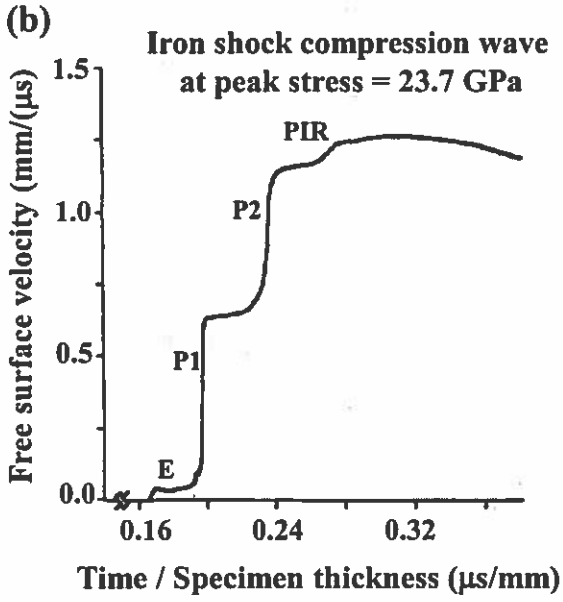

[L.M. Barker and R.E. Hollenbach, JAP 45, 4872 (1974)]

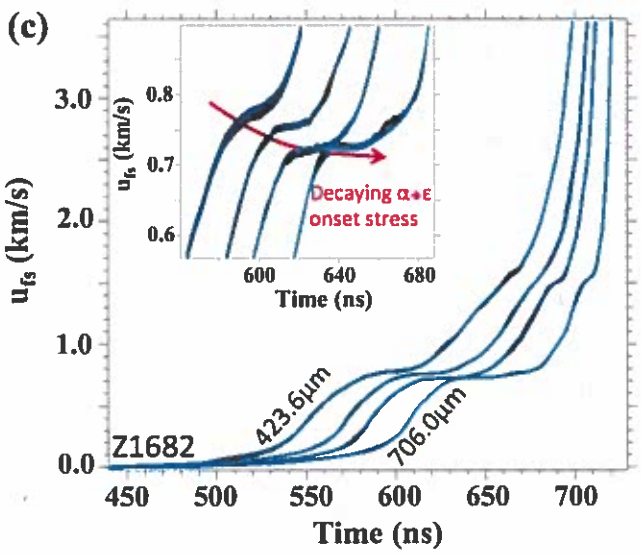

[R.F. Smith et al., JAP 114, 223507 (2013)]

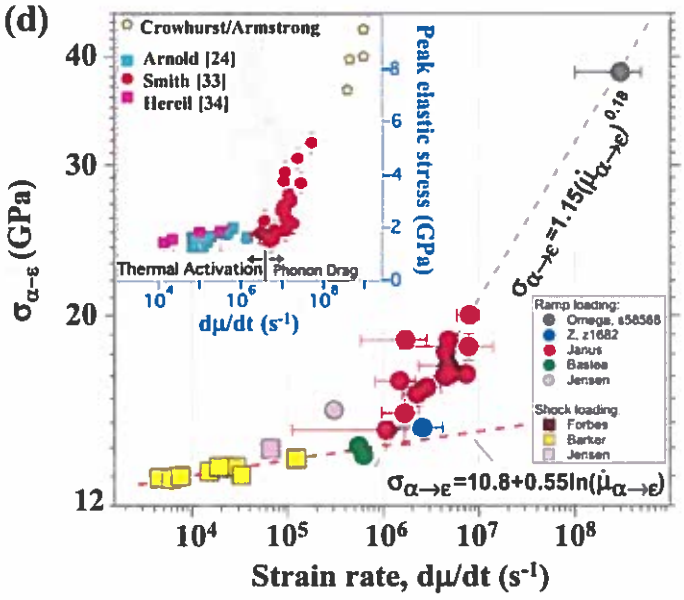

[R.F. Smith et al., JAP 114, 223507 (2013)]

Figure 1

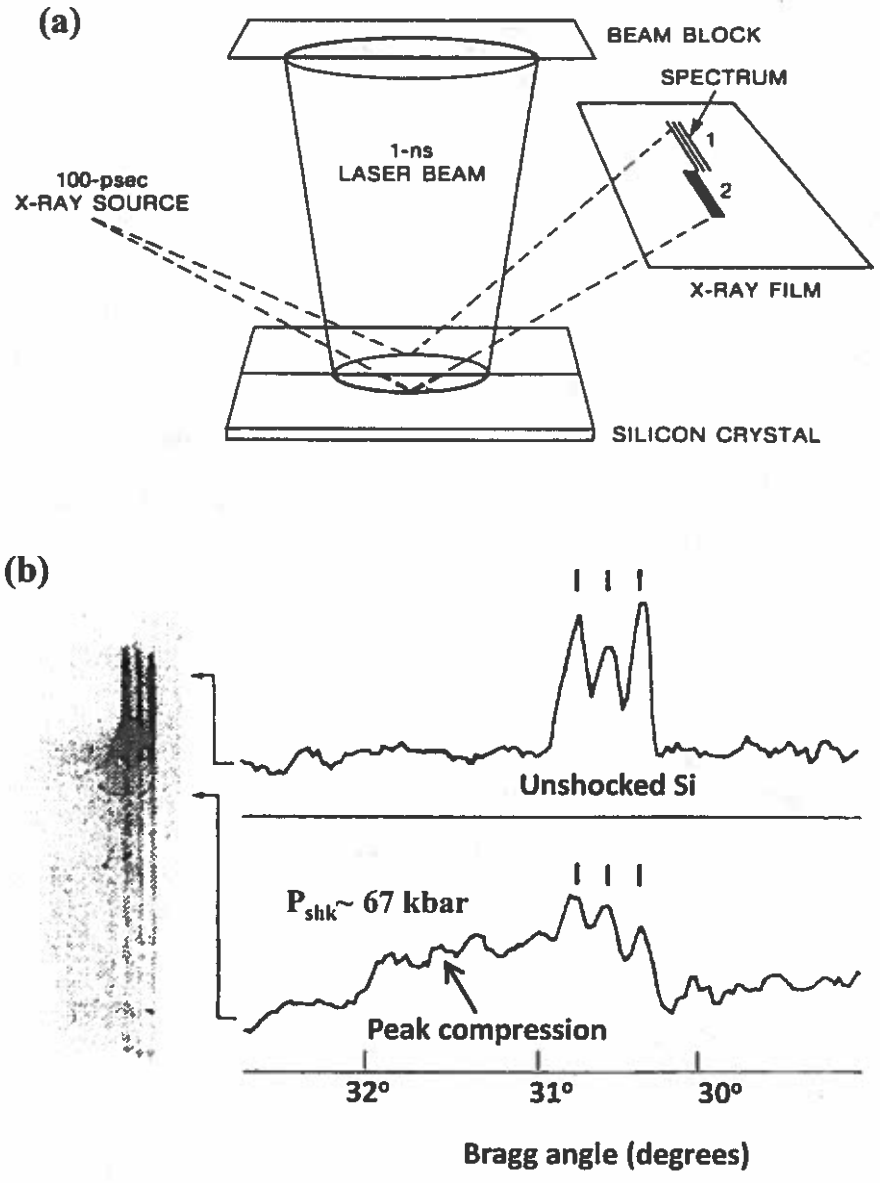

Figure 2

[J.S. Wark et al., PRB Rapid Commun. 35, 9391 (1987)]

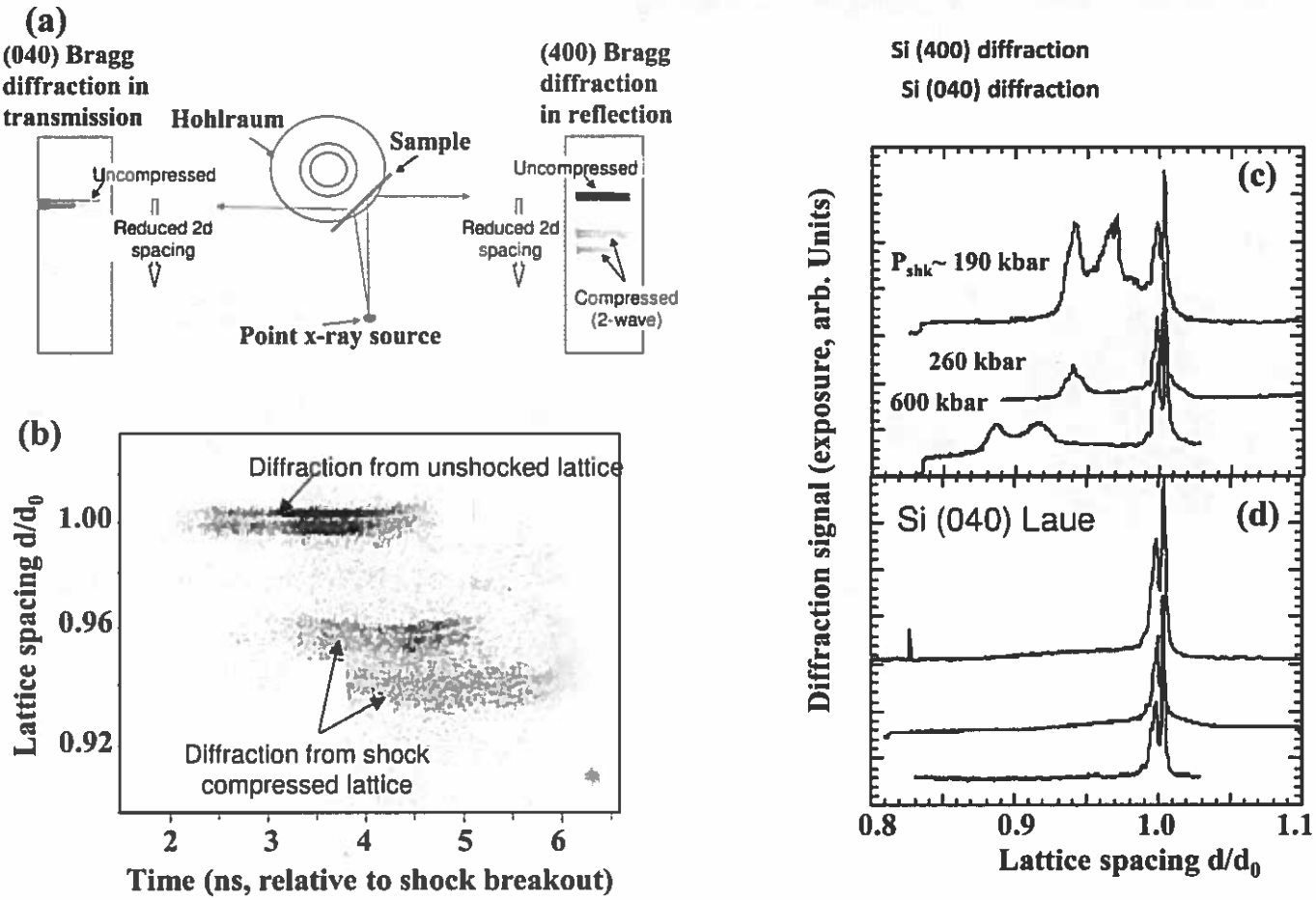

Figure 3

[Loveridge-Smith, Wark PRL 86, 2349 (2001)]

(a)

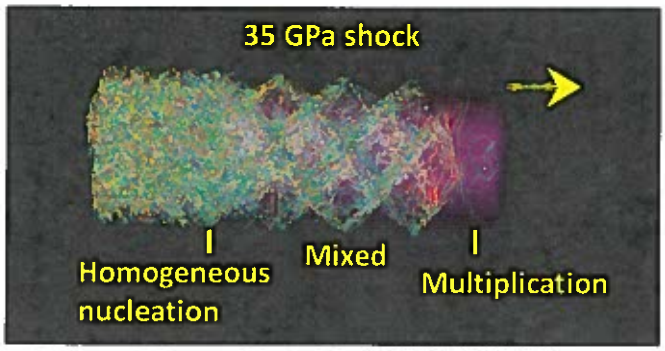

[Bringa, Nature Materials 5, 805 (2006)]

(b)

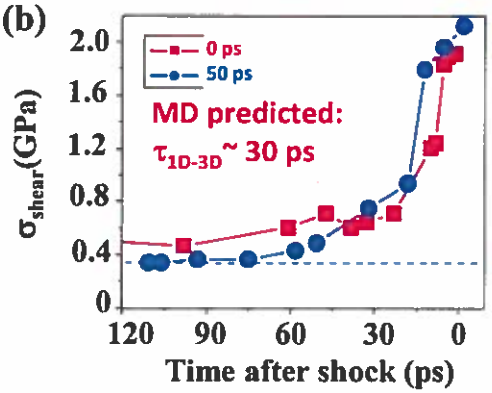

(c)

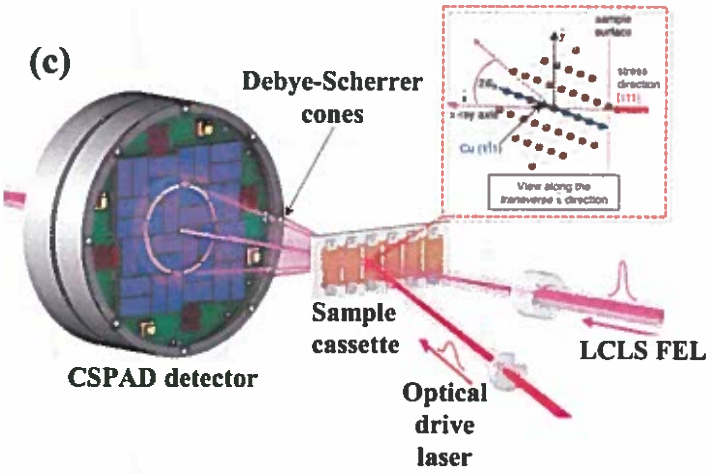

(d)

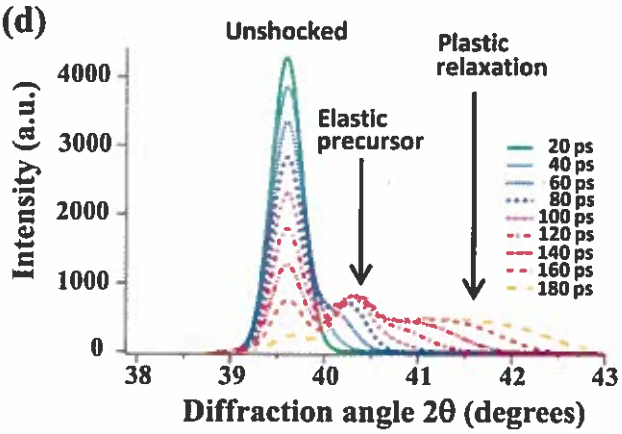

(e)

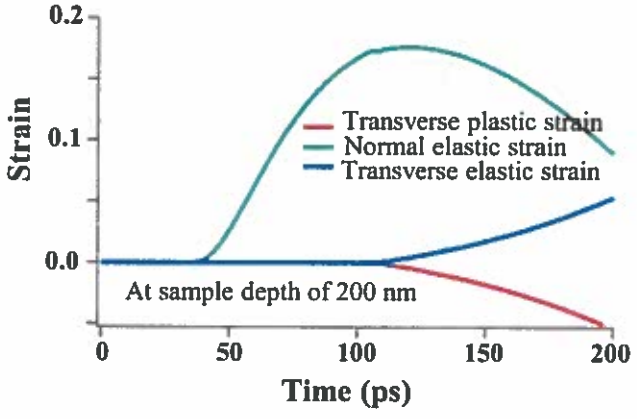

[Despina Milathianaki et al., Science 342, 220 (2013)]

(f)

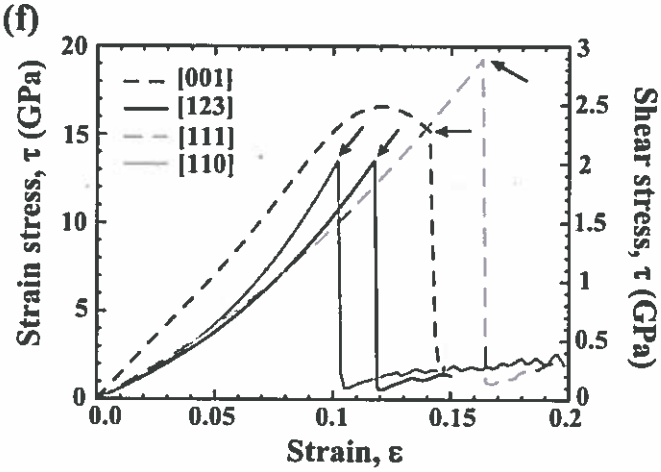

[Virginie Dupont and Timothy C. Germann, PRB 86, 134111 (2012)]

Figure 4

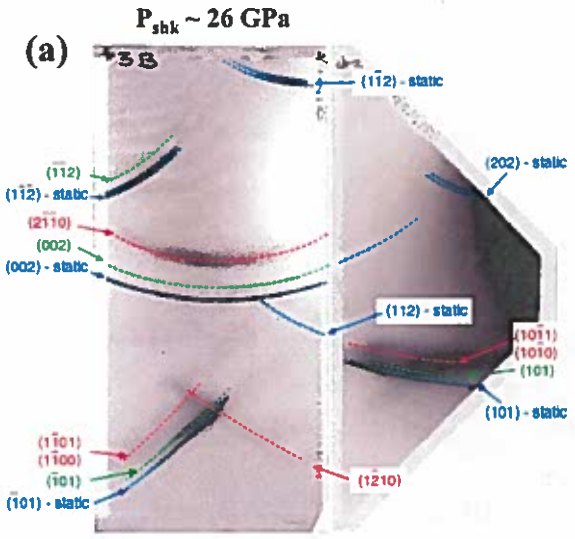

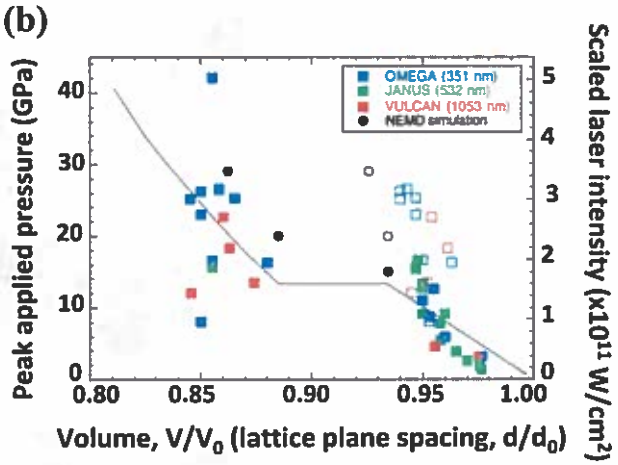

[D.H. Kalantar et al., PRL 95, 075502 (2005);
J.S. Wark et al., Proc. SCCM-07, (2007), p.286;
J. Hawreliak et al., PRB 74, 184107 (2006);

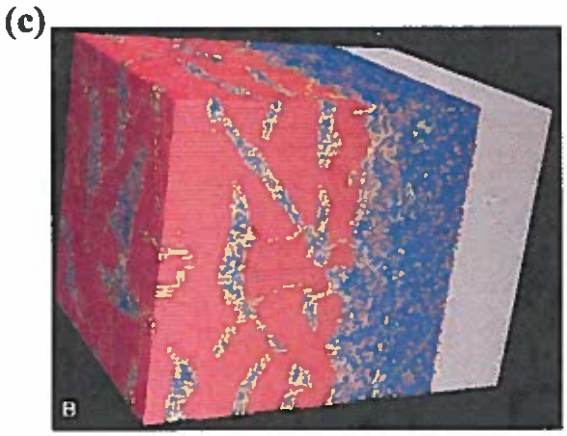

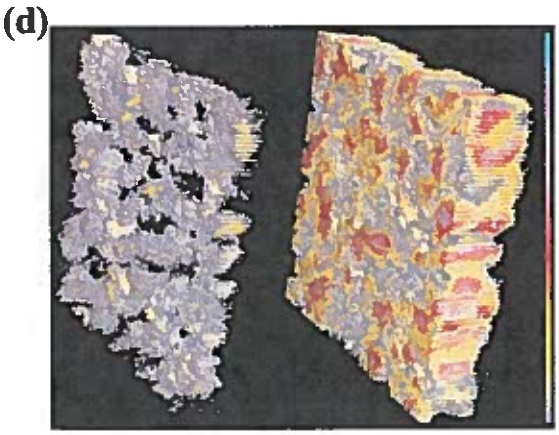

[Kai Kadau et al., Science 296, 1681 (2002)]

Figure 5

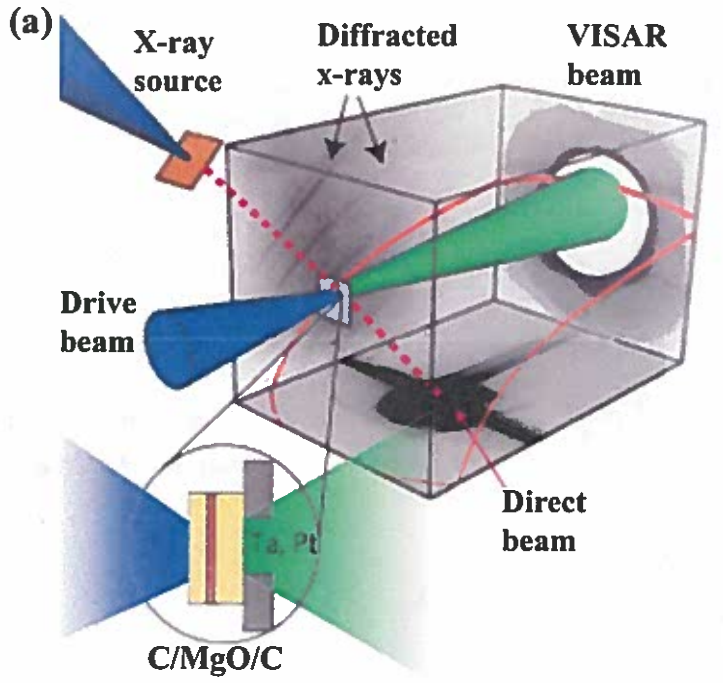

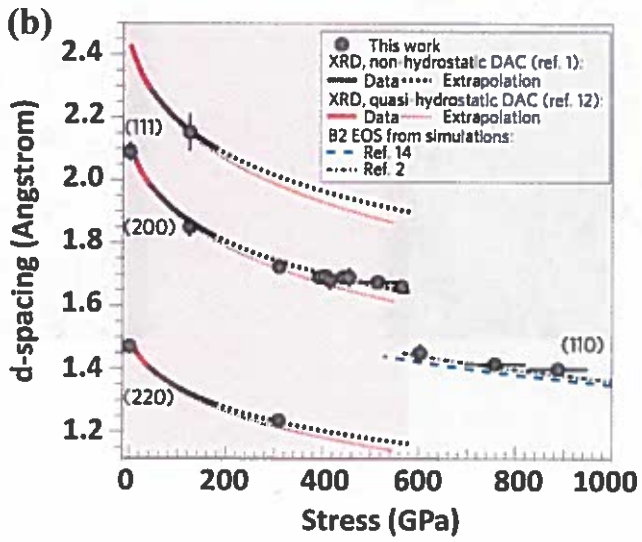

Figure 6

[F. Coppari et al., Nature Geoscience 6, 926 (2013)]

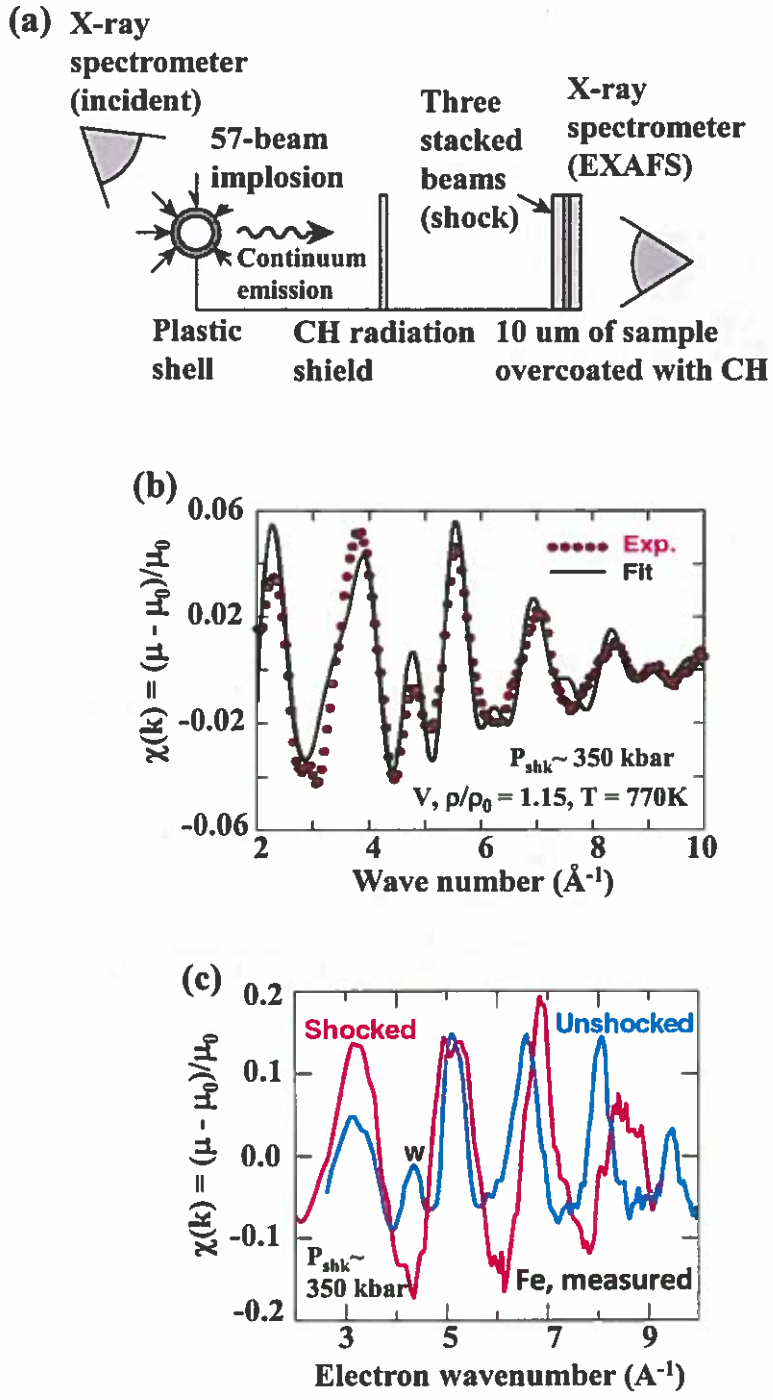

Figure 7

[Yaakobi et al., PRL 92, 095504 (2004); PoP 11, 2688 (2004); PRL 95, 075501 (2005)]

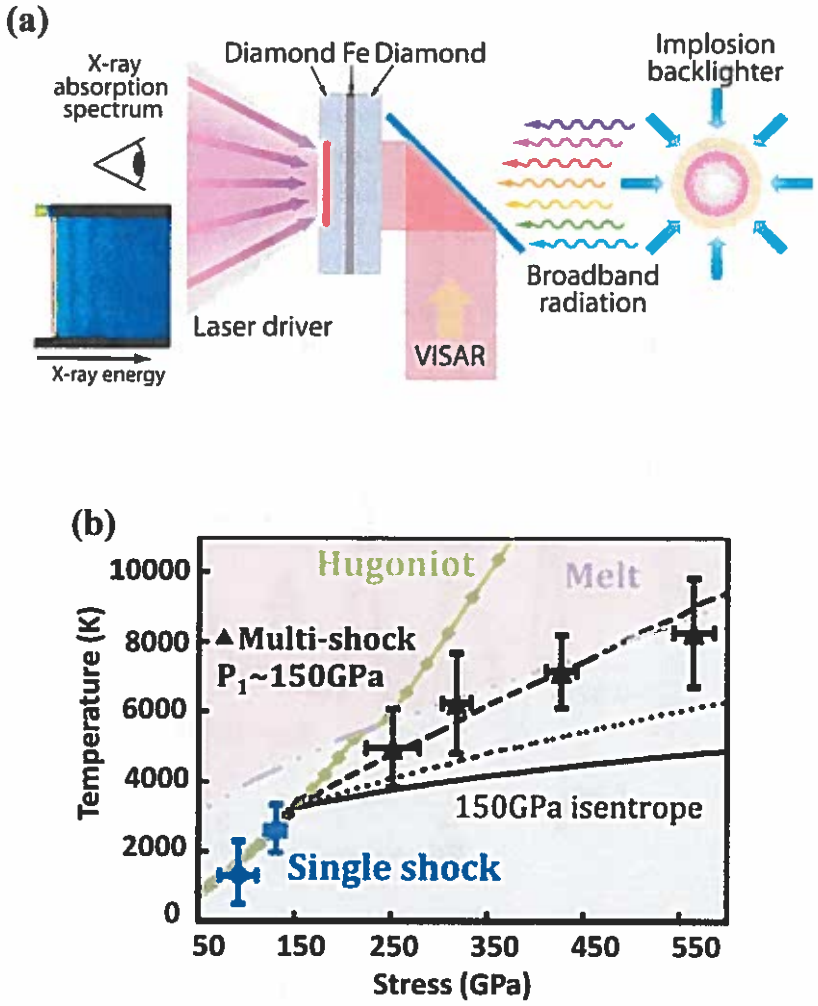

Figure 8

[Yuan Ping, PRL 111, 065501 (2013)]

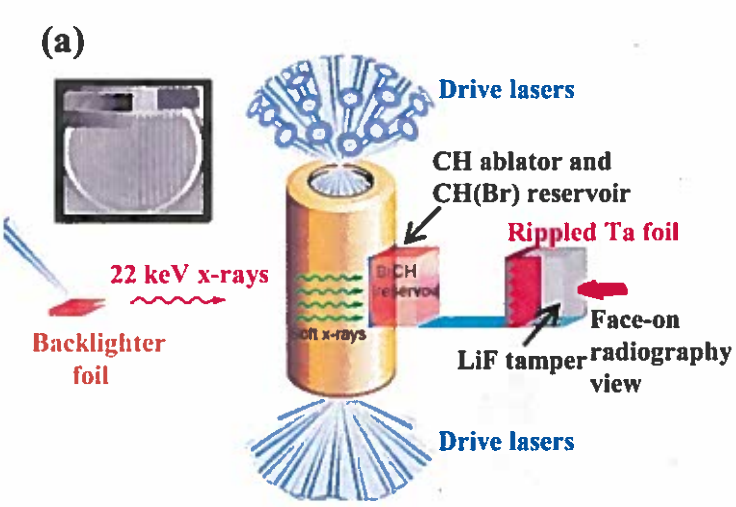

[Hye-Sook Park, PRL, in press (2015)]

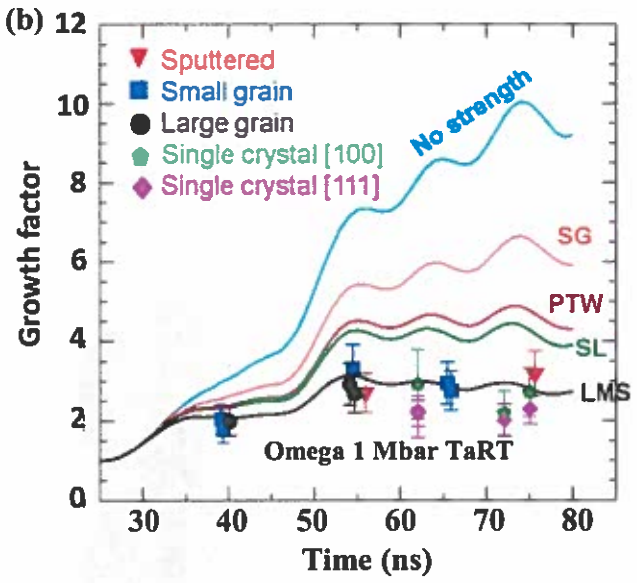

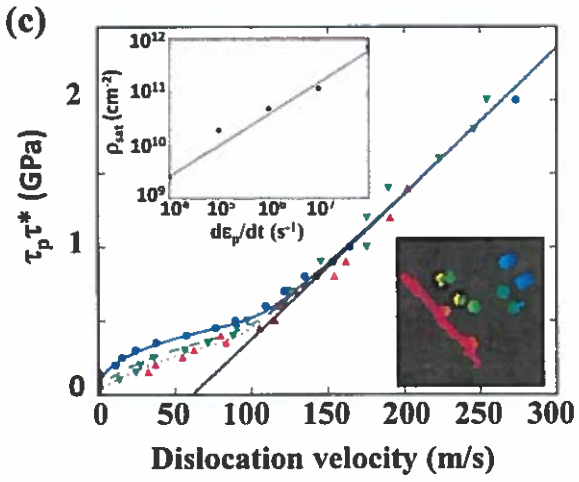

[Rudd, SCCM (2014)

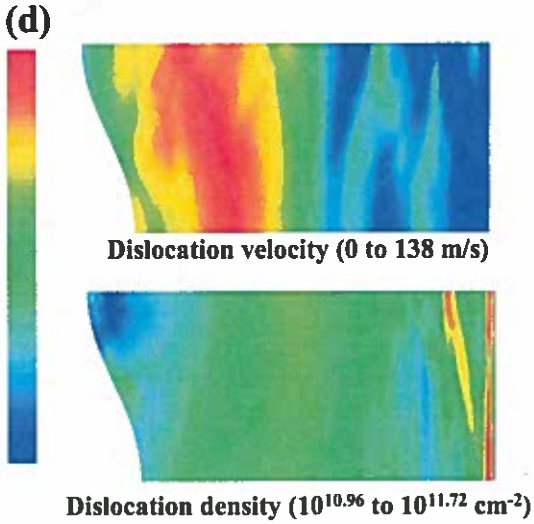

[N.R. Barton et al., JAP 109, 073501 (2011); N.R. Barton and Moon Rhee, JAP 114, 123507 (2013)]

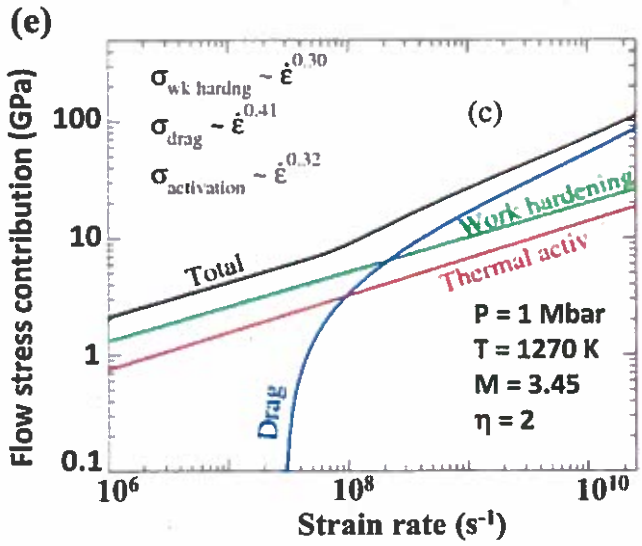

[Remington, SCCM (2012)

Figure 9

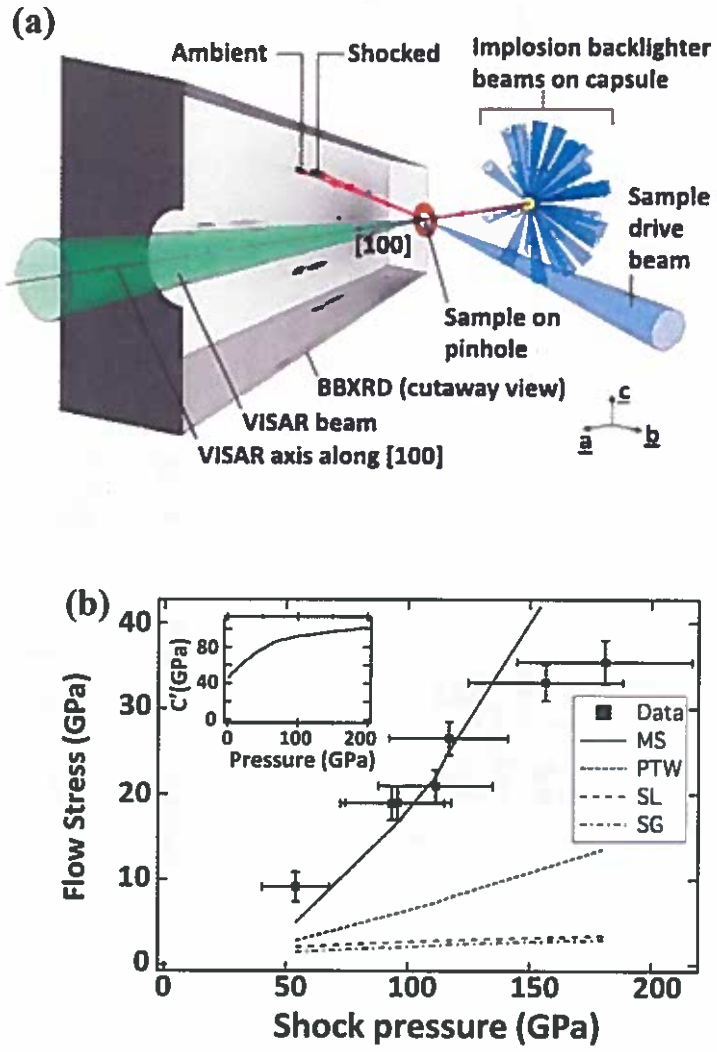

Figure 10

[Andrew Comley, PRL 110, 115501 (2013)]

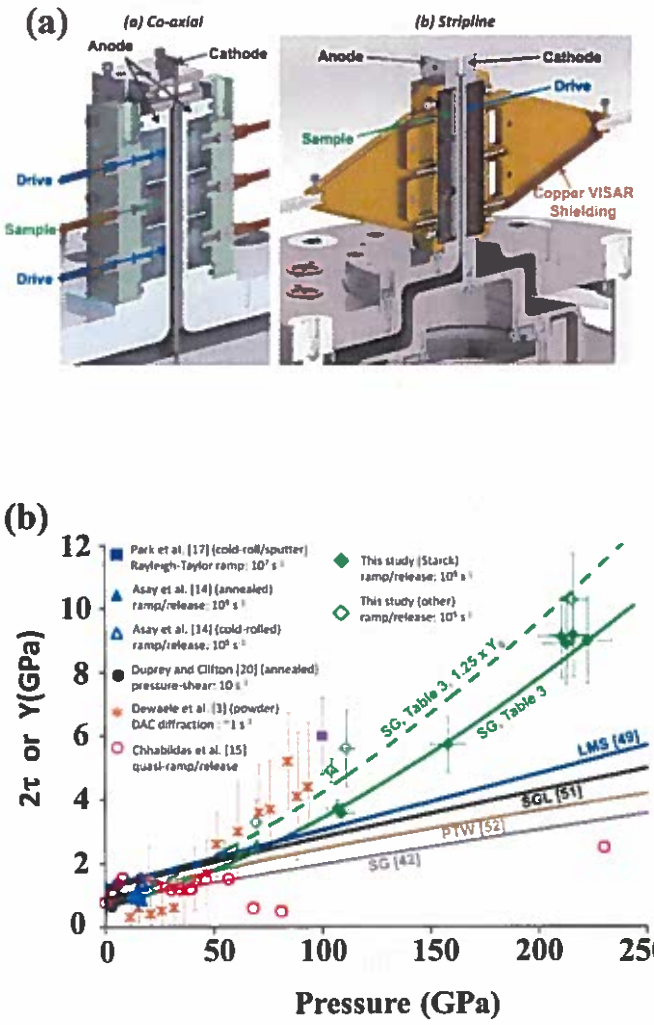

Figure 11

[Justin L. Brown et al., JAP 115, 043530 (2014)]

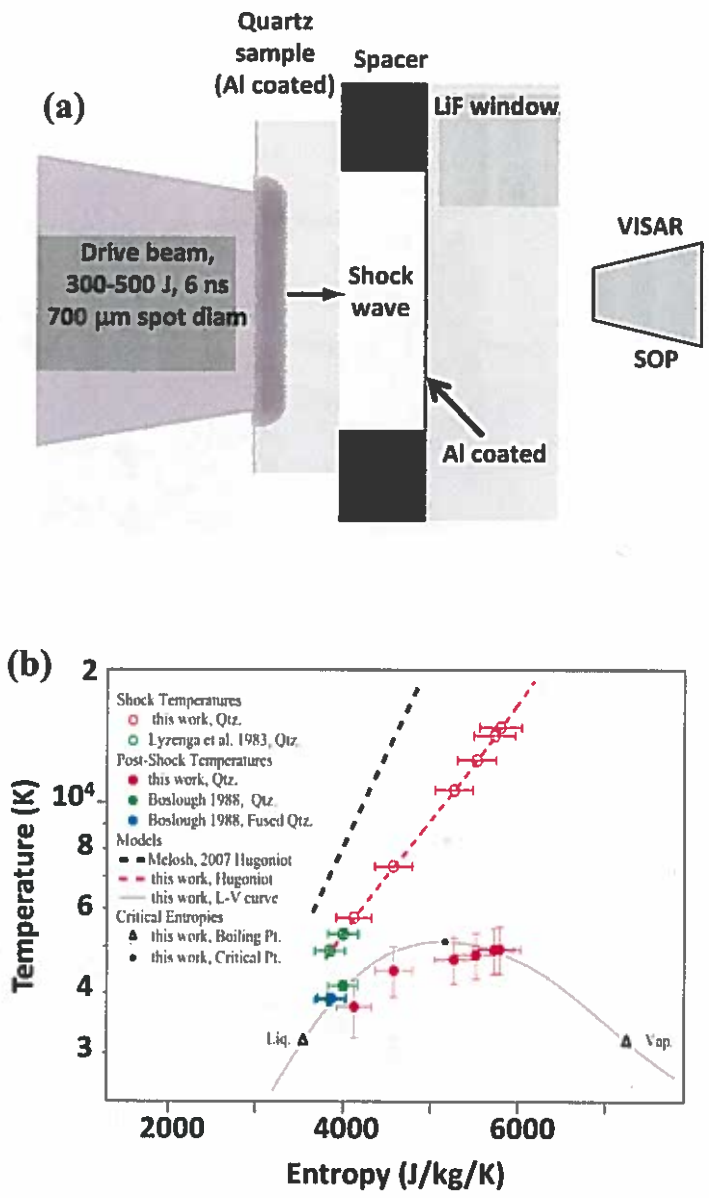

Figure 12

[R. G. Kraus, S. T. Stewart et al., JGR 117, E09009 (2012)]

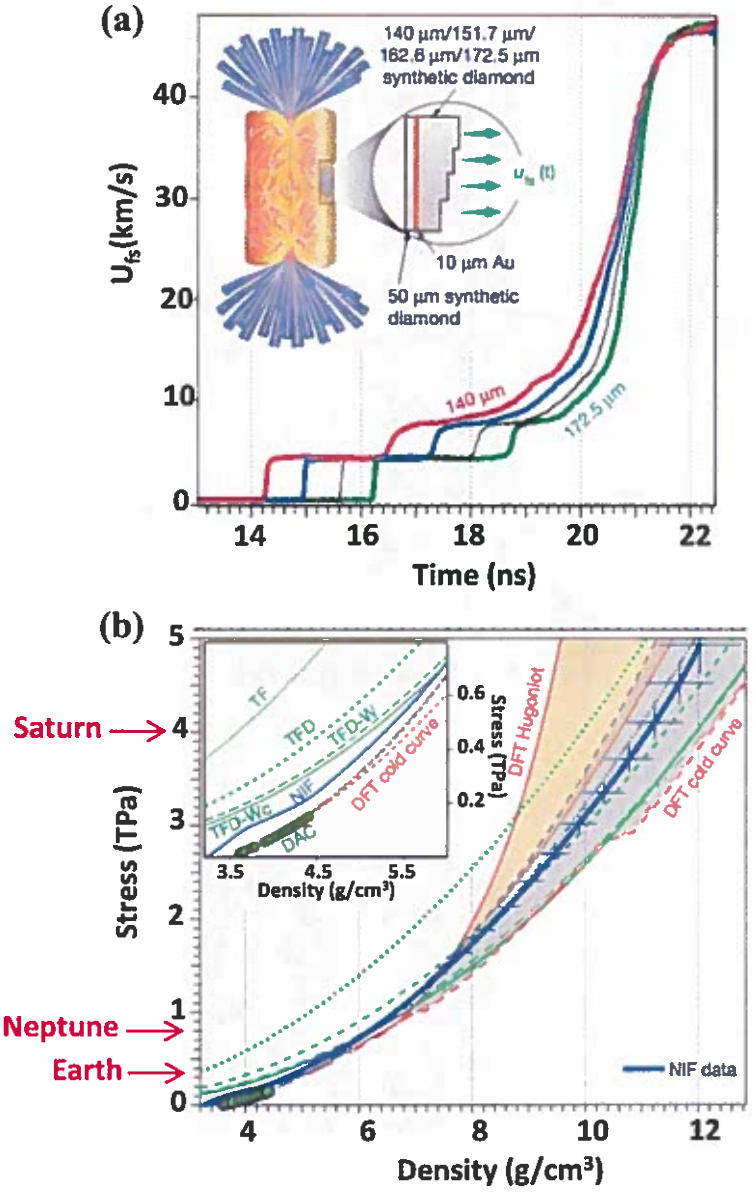

Figure 13

[R.F. Smith et al., Nature 511, 330 (2014)]

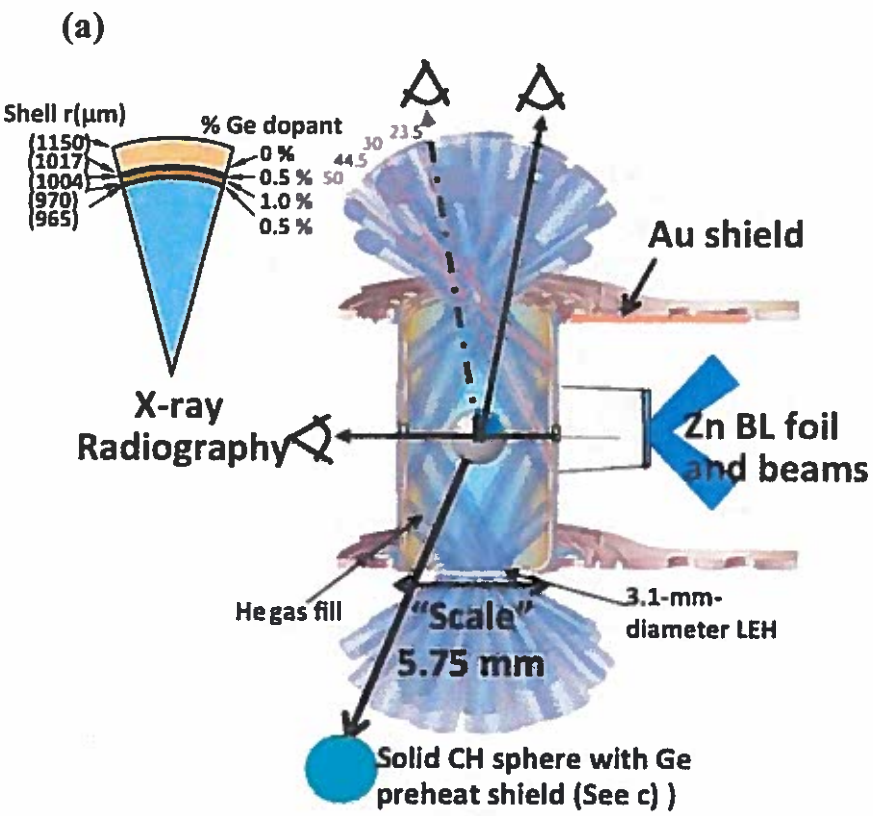

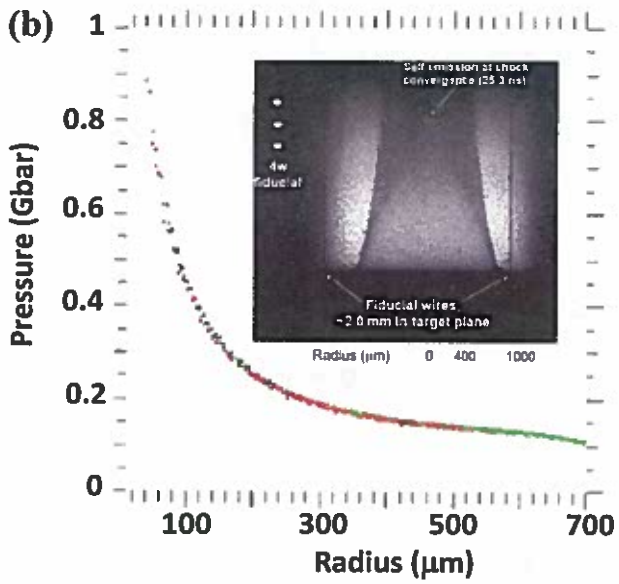

[A.L. Kritcher et al., HEDP 10, 27 (20114]

Figure 14